

Earth and Space Science



RESEARCH ARTICLE

10.1029/2020EA001590

Physically Based Summer Temperature Reconstruction From Melt Layers in Ice Cores

Key Points:

- A novel method to reconstruct summer temperatures from melt layers by a numerical model is developed and applied to four ice cores
- Nonlinear relations between summer temperature and melt layer thickness suggest that a traditional linear approximation is not applicable
- Relation between summer temperature and melt layer thickness is affected by annual temperature range, annual precipitation and firn albedo

Supporting Information:

Supporting Information may be found in the online version of this article.

Correspondence to:

K. Fujita,
cozy@nagoya-u.jp

Citation:

Fujita, K., Matoba, S., Iizuka, Y., Takeuchi, N., Tsushima, A., Kurosaki, Y., & Aoki, T. (2021). Physically based summer temperature reconstruction from melt layers in ice cores. *Earth and Space Science*, 8, e2020EA001590. <https://doi.org/10.1029/2020EA001590>

Received 3 DEC 2020
Accepted 10 JUN 2021

Koji Fujita¹ , Sumito Matoba² , Yoshinori Iizuka² , Nozomu Takeuchi³ , Akane Tsushima³ , Yutaka Kurosaki² , and Teruo Aoki⁴ 

¹Graduate School of Environmental Studies, Nagoya University, Nagoya, Japan, ²Institute of Low Temperature Science, Hokkaido University, Sapporo, Japan, ³Graduate School of Science, Chiba University, Chiba, Japan, ⁴National Institute of Polar Research, Tokyo, Japan

Abstract Previous reconstructions of summer temperatures from ice cores have relied on a statistical relationship between a melt layer and temperature observed at nearby stations. This study presents a novel method for reconstructing summer temperatures from melt layers in ice cores using an energy balance model that incorporates heat conduction and meltwater refreezing in the firn. We use the seasonal patterns in the ERA-Interim reanalysis data set for an ice core site to calculate the amounts of refreezing water within the firn under various summer mean temperature (SMT) and annual precipitation conditions, and prepared calibration tables containing these three variables. We then estimate the SMTs from the refreezing amount and annual accumulation, both of which can be obtained from an ice core. We apply this method to four ice cores that were recovered from sites with different climates: two sites on the Greenland Ice Sheet, one in Alaska, and one in Russian Altai. The reconstructed SMTs show comparable variations with those of observed temperatures at nearby stations. The nonlinear relationship between SMT and melt layer thickness differs between sites, indicating that a single linear approximation cannot be employed to estimate SMT. Sensitivity analyses suggest that the annual temperature range, amount of annual precipitation, and firn albedo (which is a time-invariant value in the model) significantly affect the relationship between SMT and melt layer thickness. This new method provides an alternative to existing approaches and yields an independent estimate of SMT from ice cores that have been affected by melting.

Plain Language Summary Melt layers in ice cores have been widely used as a proxy for summer temperatures. Previous studies established a statistical relationship between melt layer thickness and temperature observed at nearby stations and then applied it to the deeper part of the ice core. This study presents a novel method for reconstructing summer temperatures from the melt layer thickness in an ice core using an energy balance model that incorporates heat conduction and meltwater refreezing in the firn. We calculate the refreezing amounts within the firn under various summer mean temperature (SMT) and annual precipitation conditions, for which a reanalysis data set is systematically changed. We then estimate the SMTs from the refreezing amount (estimated from melt layer thickness) and annual accumulation, both of which can be obtained from an ice core. We apply this method to four ice cores recovered from different climatic sites. The reconstructed SMTs show comparable variations with those of observed temperatures at nearby stations. The relationship between SMT and melt layer thickness differs between sites, indicating that a single approximation cannot be employed to estimate SMT. This new method provides an alternative independent estimate of SMT from ice cores affected by melting.

1. Introduction

Ice cores drilled on alpine glaciers and polar ice sheets contain information on environmental conditions that helps us to understand climate change. In particular, water stable isotopes (WSIs) have been utilized as a proxy of temperature, which is one of the most fundamental climatological parameters recorded in ice (e.g., Jouzel et al., 1997; Johnsen et al., 2001). However, uncertainties exist because the isotope information in ice is commonly biased by the seasonality and amount of precipitation, as well as the source of water vapor (e.g., Pfahl & Sodemann, 2014; Steig et al., 1994). Furthermore, the relationship between temperature and stable water isotopes varies from region to region, making it necessary to establish the relationship at the ice-core site to reconstruct temperature from WSIs in the ice core.

© 2021. The Authors. Earth and Space Science published by Wiley Periodicals LLC on behalf of American Geophysical Union.
This is an open access article under the terms of the [Creative Commons Attribution License](https://creativecommons.org/licenses/by/4.0/), which permits use, distribution and reproduction in any medium, provided the original work is properly cited.

On the other hand, melt layer (also called melt feature) has been widely used as a proxy for summer temperatures (e.g., Fisher & Koerner, 1994; Herron et al., 1981; Koerner, 1977; Koerner & Fisher, 1990). Trusel et al. (2018) demonstrated that melt layer could be used for estimating runoff from the Greenland Ice Sheet by combining melt layer stratigraphy with regional climate model output. Previous studies have reported warming trends based on an increase in melt layer thickness in ice cores, but few studies have quantitatively reconstructed the temperature itself (e.g., Alley & Anandakrishnan, 1995; Henderson et al., 2006; Kameda et al., 1995; Okamoto et al., 2011; Winski et al., 2018). Temperatures have generally been inferred from melt layers via an approximation formula (linear in many cases) that has been established between the observed temperatures at nearby stations and melt layers. However, there is no guarantee that such a relationship persisted in the past. Given that the melt layer is formed by melting and refreezing, its thickness directly relates to the heat balance on the glacier/ice-sheet surface.

In this study, we therefore aimed to establish a novel approach for reconstructing summer temperature from melt layers based on physical parameters that can be observed in an ice core. The melting rate of the snow/ice surface is largely a function of air temperature (Ohmura, 2001). The meltwater generated at the surface percolates downwards and encounters cold snow/firn and refreezes, often forming ice layers (called melt layers in this study), as there are internal horizons that precondition faster and slower water percolation (Wever et al., 2016). We first calculated amount of refreezing water using an energy mass balance model and reanalysis climate data, from which summer mean temperature (SMT, average of June, July, and August) is retrieved. SMTs were then inversely estimated from the SMT—melt layer thickness relationship. We applied this method to four ice cores recovered from Northern Hemisphere sites with a range of climates. We also performed sensitivity analyses to understand which climatological variables affected the relationship between reconstructed SMT and the melt layer thickness.

2. Methods and Data

2.1. Calculation Procedure

We first create calibration tables for each ice-core site, which consist of refreezing amount calculated with different combinations of SMT and precipitation. By referring to the calibration table with ice-core-derived amounts of annual accumulation and refreezing water, we estimate SMT. To generate the calibration tables, annual precipitation and SMT are systematically changed as controlled variables. As the seasonal patterns of air temperature and precipitation strongly affect snow melting and therefore refreezing amount (Fujita, 2008; Sakai & Fujita, 2017), for every ice-core site, we obtain 35 calibration tables with the input variables from 1979 to 2013 (35 years). We determine SMTs from the 35 calibration tables with a given set of annual precipitation and refreezing amount, which correspond to accumulation and melt layer thickness in an ice core. Then, an SMT is estimated as the average of the 35 SMTs derived from the different 35-year seasonal patterns. The calculation procedure is depicted as a schematic block diagram in Figure S1. For further analysis, the same procedure is also performed for positive degree day (PDD) instead of SMT.

2.1.1. Calibration Table

We use daily forcing values from the ERA-Interim reanalysis data set (Dee et al., 2011). The air temperature at the ice-core site is estimated by the pressure-level air temperatures at the closest geopotential heights containing the site elevation (Sakai et al., 2015). The input daily values of air temperature and precipitation for a given year are defined as follows:

$$\begin{aligned} T_d &= T_e - T_E + T_C, \\ P_d &= \frac{P_C}{P_E} P_e, \end{aligned} \quad (1)$$

here T and P denote air temperature and precipitation, respectively. The subscripts d and e denote the daily variables of the model input (d) and ERA-Interim (e), respectively; and the subscripts E and C denote the summer means for T and annual sums for P of ERA-Interim (E) and controlled variable (C), respectively. The other variables (wind speed, relative humidity, and solar radiation) are taken directly from the ERA-Interim data set.

The initial firn temperature is assumed to be the mean annual air temperature from the surface to 100 m depth, and the surface energy balance and firn temperature profile are calculated with the fixed temperature at the 100-m depth for 21 times with the same annual pattern to obtain an equilibrated temperature profile for each combination of T_C and P_C . An amount of refreezing water is then obtained under the controlled SMT (T_C) and annual precipitation (P_C). The controlled SMT is varied from -15°C to $+5^\circ\text{C}$ at an interval of 1°C , and the controlled annual precipitation is varied from 100 mm to the maximum annual accumulation in a specific ice core at an interval of 20 mm.

We estimate SMT with the annual accumulation (P_i , mm w.e.) and amount of refreezing water (W_i , kg m^{-2}) of a specific ice core by referring the calibration tables, which consist of SMT, annual precipitation, and refreezing amount. The refreezing amount (W_i) is obtained from the melt layer thickness (D_i , mm) in the annual layer with firn density (ρ_f , kg m^{-3}) as follows:

$$W_i = (\rho_i - \rho_f) \frac{D_i}{1000}, \quad (2)$$

here ρ_i is the ice density (900 kg m^{-3}), we assume an initial firn density of $450 \pm 100 \text{ kg m}^{-3}$ before meltwater percolating. The uncertainty of firn density (100 kg m^{-3}) directly affects the SMT uncertainty (Section 2.1.3).

2.1.2. Forward Estimation by Biasing ERA-Interim Temperature

For cross-checking the method described above, we estimated SMT via an alternative approach that uses the same model with the same ERA-Interim input, for which Equation 1 is modified as:

$$\begin{aligned} T_d &= T_e + dT, \\ P_d &= r_P P_e, \\ r_P &= \frac{P_i}{P_E}, \end{aligned} \quad (3)$$

here dT is the temperature bias ($^\circ\text{C}$) for the ERA-Interim temperature. The ERA-Interim precipitation (P_e) is calibrated with a precipitation ratio (r_P) defined as the ratio of P_i to the annual ERA-precipitation (P_E , mm). Both P_i and P_E are averaged for the period with available data (from 1979 to the year each ice core was drilled, Table 1). With the biased temperature and calibrated precipitation, we calculate the annual refreezing amounts (W_i , kg m^{-2}) using the same energy-mass balance model by varying the input temperature with dT , and then obtain root mean square error (RMSE) and mean error (ME) against the annual refreezing amounts estimated from each ice core (W_i). We determine the temperature bias (dT) that would yield zero ME, and then obtain the biased SMT (SMT_{BIAS}). This approach is limited by the availability of the reanalysis data (since 1979, in the case of the ERA-Interim data set) and therefore cannot be used as the principal method for reconstructing SMT. This routine, which is also depicted in Figure S1, can be used to get more insights in how the original approach works and what biases are expected.

2.1.3. Uncertainty of the Estimated SMTs

While recognizing that many assumptions and parameterizations both in the ice core data and in the model are potential uncertainty contributors to the estimated SMT values, we analyze the contribution of two uncertainty sources, namely: (1) uncertainty in the estimated amount of refreezing water in the ice core, reflecting the assumed firn density before meltwater percolation and refreezing; and (2) uncertainty arising from the 35 calibration tables being calculated with different seasonal patterns. We evaluate the uncertainty due to the assumed density (σ_d , $^\circ\text{C}$) by varying the firn density from 350 to 550 kg m^{-3} . The refreezing amount is significantly altered by the seasonal pattern in the input meteorological variables, even under the same combination of annual precipitation and SMT, which we demonstrate below in our sensitivity analysis (Section 2.4). We represent the uncertainty arising from the seasonality of input variables as the standard deviation of the estimated SMTs with the 35-year patterns of ERA-Interim (σ_s , $^\circ\text{C}$). The uncertainty in the estimated SMT is finally obtained as a quadratic sum of the two uncertainties ($\sigma_T = \sqrt{\sigma_d^2 + \sigma_s^2}$, $^\circ\text{C}$). Additional causes of uncertainty are: (3) meltwater percolation into the previous annual layer; and (4) water

Table 1
Details of the Four Ice Cores Used in This Study

Ice core site	Sigma-A	SE-Dome	Aurora	Belukha
Region	Northwest Greenland	Southeast Greenland	Central Alaska	Russian Altai
Latitude (°N)	78.05	67.18	63.52	49.81
Longitude (°)	292.37	323.63	213.46	86.56
Altitude (m a.s.l.)	1500	3190	2830	4100
Year the ice core drilled	2016	2014	2008	2003
Ice core depth (m)	60.1	90.5	180.2 ^a	171.3 ^a
Firn temperature at 10 m depth (T_{10m} , °C)	-19.9	-20.6	-2.1	-14.6
Firn density at 10 m depth (kg m^{-3})	580	530	630	550
Depth at density reaching 870 kg m^{-3} (m)	>60.1	86.8	67.0	45.3
Coverage year ^b	1902	1956	1960	1914
Dating method	Seasonal changes in δD and Na^+	$\delta^{18}\text{O}$ comparison with model outputs	Seasonal changes in δD and Na^+	Pollen identification
Age markers	Tritium and SO_4^{2-}	Tritium and SO_4^{2-}	Tritium, Cl^-/Na^+ , and SO_4^{2-}	Tritium
Dating error	± 1 year	± 2 month	± 3 year	± 3 year
Method for melt layer measurement	Image analysis of transmitted light photograph	Visible inspection and X-ray density	Visible inspection on a light table	Visible inspection on a light table
Mean melt layer thickness (D_i , mm)	28 ± 57	4 ± 6	77 ± 79	54 ± 51
Mean annual accumulation rate of ice core (P_i , mm w.e.)	314	1058	1495	399
Mean annual precipitation of ERA-Interim (P_E , mm)	197	1011	717	810
Precipitation ratio (r_P)	1.60	1.05	2.09	0.49
ERA-Interim summer mean temperature (T_E , °C)	-2.25 ± 1.45	-8.34 ± 1.10	-2.42 ± 1.02	-3.51 ± 0.70
Bias for ERA-Interim temperature (dT , °C)	-1.52 ± 0.28	$+0.45 \pm 0.29$	-0.37 ± 0.30	$+2.35 \pm 0.27$
References for ice core	Matoba et al. (2018); Kurosaki et al. (2020)	Iizuka et al. (2016); Furukawa et al. (2017)	Tsushima et al. (2015)	Takeuchi et al. (2004); Okamoto et al. (2011); Aizen et al. (2016)

^aThe ice core is not fully used for this study. ^bYear to which melt layers are analyzed.

refreezing without forming ice lens. We discuss these contributions to the uncertainty qualitatively (Section 4.1) because these are hard to formalize and quantify.

2.2. Model

For quantifying the relationship between SMT and melt rate, we utilize an energy mass balance model (GLacIer energy Mass Balance model: GLIMB) that was originally developed for a Tibetan glacier (Fujita & Ageta, 2000; Fujita et al., 2007). The model consists of the surface and subsurface parts. The surface part calculates the surface energy balance at a daily time step. The subsurface part calculates the conductive heat and temperature changes in the glacier firn and ice as well as the refreezing of percolating meltwater, which has been shown to play a key role in the mass balance of a cold glacier in central Tibet (Fujita et al., 1996, 2000). Time and depth steps are 1-h and 0.1 m, respectively. Forcing variables are air

temperature, wind speed, relative humidity, solar radiation, and precipitation. GLIMB has been applied to glaciers across a range of climates in High Mountain Asia (e.g., Fujita et al., 2011; Fujita & Nuimura, 2011; Fujita & Sakai, 2014; Sakai et al., 2010, 2015).

2.2.1. Surface Energy Balance

The model solves the surface energy balance (Q , W m^{-2}) as follows:

$$Q = (1 - \alpha_s)R_s + \varepsilon R_l - \varepsilon\sigma(T_s + 273.15)^4 + H_s + H_l + Q_g, \quad (4)$$

here α_s is the surface albedo (dimensionless), R_s is the downward shortwave radiation (W m^{-2}), R_l is the downward longwave radiation (W m^{-2}), ε is the emissivity (assumed to be 1, dimensionless) for longwave radiations. σ is the Stefan-Boltzmann constant ($5.67 \times 10^{-8} \text{ W m}^{-2} \text{ K}^{-4}$) for upward longwave radiation emitted from the surface with temperature of T_s ($^{\circ}\text{C}$). The sensible (H_s) and latent (H_l) turbulent fluxes (W m^{-2}) are estimated by a bulk aerodynamic method (Kondo, 1994). The conductive heat (Q_g) is calculated with the surface and snow temperatures as described in the next section. All components are positive when the heat fluxes are directed toward the surface. The downward longwave radiation (R_l) is calculated via an empirical equation proposed by Kondo (1994), which incorporates air temperature, relative humidity, and solar radiation. Meltwater is generated when the surface energy balance is greater than zero as:

$$\begin{aligned} Q_m &= \max[0; Q], \\ M_s &= \frac{t_d Q_m}{l_m}, \end{aligned} \quad (5)$$

here Q_m is the heat for snow melting (W m^{-2}), M_s is the daily meltwater ($\text{kg m}^{-2} \text{ day}^{-1}$ or mm w.e. day^{-1}), t_d is the duration of one day (86,400 s), and l_m is the latent heat of fusion of ice ($3.33 \times 10^5 \text{ J kg}^{-1}$), respectively. The schemes for albedo and for snow densification are described in the supporting information.

2.2.2. Heat Conduction

Subsurface in the model consists of snow and firn layers. The snow layer forms as a result of mass balance during a corresponding year and thus changes in thickness and temperature are calculated. On the other hand, the thickness and density profile of the firn layer is assumed to be unchanged, meaning that the boundary between snow and firn layers would be fixed even if the melt exceeded the accumulated snow (suggesting negative mass balance), while the temperature profile would be affected if such large amount of meltwater was supplied through the boundary. Heat conduction in the snow/firn, which is required to estimate the surface temperature and water refreezing, is calculated using the change in the temperature profile within the snow/firn as follows:

$$\rho_z c_i \frac{\partial T_z}{\partial t} = K_s \frac{\partial^2 T_z}{\partial z^2}, \quad (6)$$

here ρ_z is the snow density (kg m^{-3}), which changes along the depth from the surface, z (m). c_i is the specific heat of ice ($2100 \text{ J kg}^{-1} \text{ K}^{-1}$), T_z is the snow temperature ($^{\circ}\text{C}$) at the depth of z , and K_s is the thermal conductivity of snow/firn ($\text{W m}^{-1} \text{ K}^{-1}$), obtained as a function of snow density (Mellor, 1977) as:

$$K_s = 0.029(1 + 10^{-4} \rho_z^2). \quad (7)$$

The conductive heat is then obtained via the temperature gradient in the uppermost layer of snow (dT_s/dz , K m^{-1}) as:

$$Q_g = K_s \frac{dT_s}{dz}. \quad (8)$$

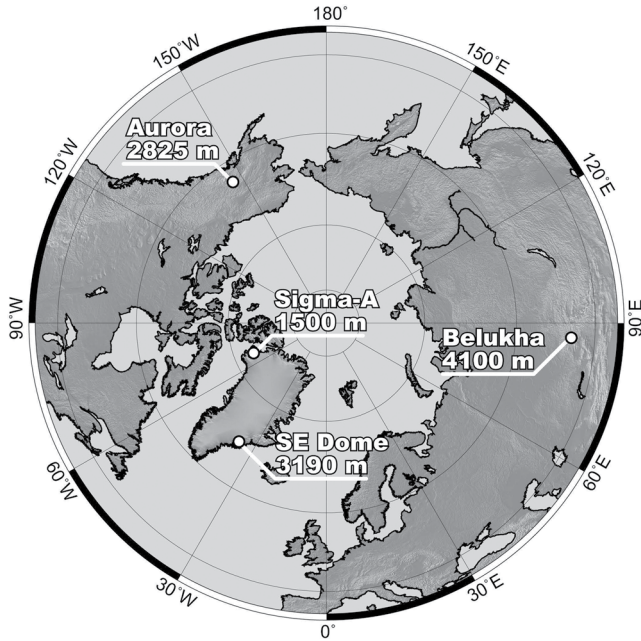


Figure 1. Locations of the ice-core sites. See also Table 1.

In this model, we calculate the temperature profile ($dT_s = T_{z=0.1m} - T_s$) throughout the snow layer at an interval of 0.1 m ($dz = 0.1$ m). When the surface is wet with meltwater or rainwater, the heat transfer in snow becomes zero. We employ a one hour time step to calculate the heat conduction.

2.2.3. Water Refreezing

Water percolation, in which not only meltwater but also rain and condensation water are taken into account, is calculated by a commonly used bucket water routine scheme: water is allowed to enter each next layer as the current layer cannot retain more water by capillary forces. The maximum water content (w_c , %), which constrains how much water the snow layer can retain, is determined by the Monte Carlo simulation (Section 2.2.4).

The amount of refreezing water (W_r), which forms the melt layer, is calculated for three cases: (1) water percolating into the cold snow layer, (2) water that is retained in the snow and refrozen by the underlying cold snow, and (3) water that is retained in the snow and refrozen by cold events or the coming winter. Case 1 can be described by the temperature of cold snow and the amount of percolated water as follows:

$$W_r = \min \left[-\frac{\rho_z c_f T_z dz}{l_m}; W_z \right], \quad (9)$$

here W_z is percolated water (kg m^{-2}) in a given snow layer at the depth of z . Both cases 2 and 3 are described as the heat transfer between wet and dry (cold) layers as follows:

$$W_r = \min \left[-t_d K_s \frac{T_z'}{l_m dz}; W_z \right], \quad (10)$$

here T_z' is the temperature of a given snow layer that is in contact with the wet snow layer at the depth of z , which can be below (case 2) or above (case 3) the wet snow layer. If the wet layer is located just below the surface, T_z' is replaced by T_s . We assume that the refreezing water alters the snow density toward the ice density. The freezing amount is constrained by how much latent heat can be absorbed in the layer (case 1) or conducted from a wet layer toward above/below cold layers (cases 2 and 3). In the calculation, we do not distinguish between these cases, and sum the calculated heat-transfer values for the three cases as refreezing water. Although the cases 2 and 3 may not necessarily result in forming ice lens but in increasing snow grain size, we assume that all refreezing water contributes to melt layer.

2.2.4. Model Calibration

We calibrate the model parameters using meteorological data from the Sigma-A site in northwest Greenland (Figure 1), where continuous observations have been acquired since July 2012 (Aoki et al., 2014; Niwano et al., 2015, 2018; Nishimura et al., 2021). We perform a Monte Carlo simulation ($n = 10,000$) by varying the 15 parameters related to albedo and densification, which would affect the processes of melting and refreezing (Table S1). We then determine their values by comparing the simulated and observed daily values of surface level and albedo for the 2012–2015 period. Daily precipitation at the Sigma-A site is estimated from the positive change of surface elevation with a certain value for fresh snow density, which is one of the varied parameters in the Monte Carlo simulation.

2.3. Ice Cores

We apply this method to four ice cores recovered from sites with different climates: Sigma-A in northwest Greenland (drilled in 2017; Matoba et al., 2018); SE-Dome in southeast Greenland (drilled in 2015; Furukawa et al., 2017; Iizuka et al., 2016, 2017, 2018); Aurora Peak in Alaska (drilled in 2008; Tsuchima

et al., 2015); and Mt. Belukha in the Russian Altai Mountains (drilled in 2003; Aizen et al., 2016; Okamoto et al., 2011; Takeuchi et al., 2004) (Figure 1 and Table 1).

At all sites, borehole temperatures and firn density suggest that there was no temperate wet firn over the timescales covered by the cores (Table 1). The 10-m firn temperature (T_{10m} , °C), which is usually assumed as the annual mean temperature in the polar regions (Epstein et al., 1963), show similar values for the two Greenland sites though the Sigma-A site is located farther north but at lower elevation than the SE-Dome site. T_{10m} at the Aurora site seems significantly warm (-2.1°C), possibly due to snow events under warm conditions. The 10-m firn densities are similar among the sites ($530\text{--}630\text{ kg m}^{-3}$) while the depth at which firn reaches ice density is different from site by site (Table 1).

The chronology and net accumulation of each ice core were determined and calibrated in the respective studies. Annual layers in the Sigma-A and Aurora ice-cores are defined between winters, while the SE-Dome ice-core is dated on a monthly scale. The Belukha ice-core is dated from pollen grains that indicate spring and autumn. The reconstructed annual accumulation (P_I) suggests that the Sigma-A and Belukha sites are in more arid condition ($300\text{--}400\text{ mm}$) than the SE-Dome and Aurora sites ($>1000\text{ mm}$). In addition, P_I and the ERA-Interim annual precipitation (P_E) show different features between sites. Not only the annual means ($r_p = P_I/P_E = 1.05$) but also the inter-annual variations are surprisingly consistent at the SE-Dome site (Furukawa et al., 2017) while precipitation of the reanalysis data set is generally underestimated at the high elevation mountain due to a coarse resolution of topography in the reanalysis model ($r_p = 1.60$ for Sigma-A and $r_p = 2.09$ for Aurora sites). Although it is unclear why the ERA-Interim precipitation was overestimated for the Belukha site ($r_p = 0.49$), the vapor might not be removed sufficiently during transportation to the Siberian inland in the reanalysis model. Although there is no study that evaluated the performance of such vapor transfer in the reanalysis data set, a study using water stable isotopes in snow suggests a significant contribution of vapor recycling to winter precipitation in the inland Siberia, which is not represented in the reanalysis data set (Kurita et al., 2004).

Melt layer thickness was observed by different methods for each ice core (Table 1). The minimum melt layer thickness is $1 \pm 1\text{ mm}$ in all of the ice cores. It is assumed that a single melt layer is formed with the water generated by melting during the corresponding year. When multiple layers are counted, their thicknesses are summed into a single layer. Horizontal advection and excess water that infiltrated from the above layer would disturb the ice-core information, regardless of the applied method. The smoothed density profile of each ice core is used to determine the thermal conductivity (Equation 7). We also use observed temperature records at nearby stations (SMT_{STA}) to validate the reconstructed/biased SMTs (Table S2).

2.4. Sensitivity Calculation

The relationship between SMT and refreezing amount is expected to depend on the climatic setting as inferred from studies on mass balance sensitivity (Fujita, 2008; Sakai & Fujita, 2017). We therefore perform sensitivity analyses with idealized meteorological inputs to better understand how this relationship is governed by the given climatic condition.

2.4.1. Idealized Meteorological Inputs

We analyze the meteorological variables in the ERA-Interim data set at three of the ice-core sites (Sigma-A, Aurora, and Belukha). We first obtain a Fourier curve fitting for a given long-term averaged variable such as wind speed, air temperature and precipitation as:

$$v_{d_y} = \bar{v} + \sum_{\kappa=1}^2 (a_{\kappa} \sin \kappa d_{\theta} + b_{\kappa} \cos \kappa d_{\theta}), \quad (11)$$

here v_{d_y} and \bar{v} are the Fourier-fit variable at a given day of year (d_y) and annual mean, respectively. The day of year is converted to the radian unit ($d_{\theta} = 2\pi(d_y/365)$). The idealized wind speed (w_s , m s^{-1}) is simply converted from the Fourier-fit curve (v_{d_y} replaced by w_{d_y}) by adding a Gaussian noise of wind speed (dw_s , m s^{-1}) as follows:

$$w_s = \max \left[w_{d_y} + dw_s; 0 \right]. \quad (12)$$

For the air temperature (v_{d_y} replaced by T_{d_y}), we add a parameter to change the annual temperature range (R_T , °C) as:

$$T_a = \frac{R_T}{|T_{d_y_max} - T_{d_y_min}|} \left(T_{d_y} - \bar{v}_T \right) + \bar{v}_T + dT_a, \quad (13)$$

here T_a is the idealized air temperature, and $T_{d_y_max}$ and $T_{d_y_min}$ are the maximum and minimum temperatures of the Fourier-fit curve (T_{d_y} , °C), respectively. \bar{v}_T is the annual mean air temperature (°C). A Gaussian noise of air temperature (dT_a , °C) is also added.

The normalized precipitation is defined as the daily precipitation divided by the annual sum (P_{d+d_d} , dimensionless), and it is described as:

$$P_{d+d_d} = \max \left[\frac{R_P}{|P_{d_y_max} - P_{d_y_min}|} \left(P_{d_y} - \bar{v}_P \right) + \bar{v}_P + dP_r; 0 \right], \quad (14)$$

$$P_r = \frac{P_{d+d_d}}{P_A},$$

here $P_{d_y_max}$ and $P_{d_y_min}$ are the maximum and minimum normalised precipitations of the Fourier-fit curve (P_{d_y} , dimensionless). \bar{v}_P is the annual mean of normalized precipitation (dimensionless). Precipitation concentration can be regulated by a parameter R_P (dimensionless). Precipitation seasonality, which expresses how the timing of precipitation peak differs from the standard condition, can be changed by a parameter d_d . A Gaussian noise of normalized precipitation (dP_r , dimensionless) is also added, and the obtained precipitation is set to zero if negative. The idealized normalized precipitation (P_r , dimensionless) is finally obtained from the above mentioned normalized precipitation divided by the annual sum of P_d (P_A , dimensionless). In order to proceed to sensitivity analyses (Section 2.4.2), we create calibration tables by systematically varying air temperature and precipitation as described by Equation 1. All Gaussian noises shown above are calculated from the standard deviations of all daily anomalies of the ERA-Interim variables.

Relative humidity and solar radiation are parameterized with the daily precipitation amount based on an analysis conducted for meteorological data at multiple sites in High Mountain Asia (Matsuda et al., 2006). We compare the residual of relative humidity ($1 - H_r$, dimensionless) and normalized solar radiation (R_s/R_t , dimensionless, where R_t is the solar radiation at the top of atmosphere) with the daily precipitation amount at the four ice-core sites. Both variables ($1 - H_r$ and R_s/R_t) can be fit to precipitation using exponential decay curves (Figure S2). The seasonal patterns of the normalized variables and of the daily variability are shown in Figure S3.

2.4.2. Variables Changed

We define an idealized ice-core setting as one with a 20-mm-thick melt layer in an annual layer that is produced from 500 mm w.e. accumulation and then evaluate how the estimated SMT varied with given variable changes. We prepare a 30-year-long daily data set (Figure S4). We test six variables, including latitude (seasonality of solar radiation, Figure S5), temperature range (R_T , Figure S6), precipitation concentration (R_P , Figure S7), and precipitation seasonality (d_d , Figure S8). Using the Fourier-based idealized meteorological input prepared above, we can test effects of individual variables independently though these variables highly relate to each other. In addition, we test the sensitivities of SMT by varying annual accumulation amount (Figure S9) and firn albedo. Once we obtain the response of SMT to the variables mentioned above, we calculate how the heat and mass budget components respond to the changing variable under a constant value of SMT (-4.58°C), which is obtained with the controlled idealized variables.

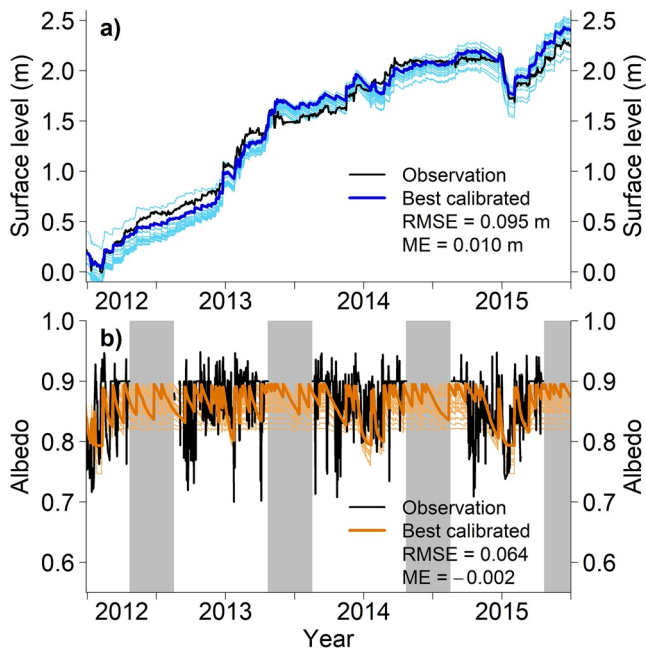


Figure 2. Temporal changes in (a) surface level and (b) albedo at the Sigma-A site, northwest Greenland, from July 2012 to December 2015. The thick solid and thin colored lines denote the best calibrated result and best 20 estimates from the Monte Carlo simulation, respectively. RMSE and ME denote the root mean square error and mean error, respectively. Gray shaded regions in (b) denote the winter (polar night) period when there were no albedo observations.

We also perform additional sensitivity tests for the 15 parameters calibrated in Section 2.2.4 (Table S1), changing these parameters to the ranges tested for the Monte Carlo simulation and obtaining temperature ranges of SMT with the idealized meteorological inputs described above.

3. Results

3.1. Model Performance

The temporal changes in surface level and albedo at the Sigma-A site in northwest Greenland are shown in Figure 2. Figure S10 shows scatter plots of the Monte Carlo simulation ($n = 10,000$), for which the most correlated relationships are selected from 15 variables (Table S1). RMSEs of surface level and albedo are highly correlated ($r = 0.571$, $p < 0.001$), and the parameters resulting in the minimum RMSE of surface level are used for the following simulations (Figure S10a). Most parameters do not correlate with the RMSEs of surface level and albedo whereas the fresh snow density ($r = -0.834$, $p < 0.001$, Figure S10b) and firn albedo ($r = -0.738$, $p < 0.001$, Figure S10c) significantly correlate with RMSEs of surface level and albedo, respectively.

With the parameters yielding the best estimate of surface level and albedo for the Sigma-A site, we calculate RMSE and ME of the refreezing amount by varying air temperature with the biased ERA-Interim precipitation at each site (Section 2.1.2). There is no significant minimum in the RMSEs as shown in Figure S11, which will be discussed in Section 4.2. We therefore determine a site-specific temperature bias (ΔT) for the ERA-Interim air temperature to yield a zero ME of refreezing amount. The calculated refreezing amount with the biased air temperature and calibrated precipitation is compared with those estimated from the ice

cores (Figure 3). The RMSE and ME in refreezing amounts (Figures S11 and 3) are related to the assumed firn density (Sections 2.1.2 and 2.3, and Equation 2).

3.2. Reconstructed SMTs

The constructed calibration tables, which are presented in Figure 4, were inversely obtained from the refreezing amounts calculated using various combinations of SMT and annual precipitation for the four ice core sites. The tables suggest that the relationships among SMT, annual precipitation, and refreezing amount vary between the study sites.

SMTs were then finally reconstructed from the calibration tables for the four ice core sites (SMT_{REC} , Figure 5, referring left axis). Also shown are the SMT anomalies recorded at nearby stations (SMT_{STA} , Table S2, referring right axis), and the ERA-biased SMT (SMT_{BIAS} , Sections 2.4.2 and 3.1, referring left axis). Two extreme cases are found in the ice cores: (1) annual layers consisting entirely of ice (orange bars at the upper part of each panel), and (2) annual layers without a melt layer (blue bars at the lower part of each panel). Correlation coefficients among SMTs (reconstructed, ERA-biased, and station) are summarized in Tables S3–S6. The SMT_{REC} for the Sigma-A site shows significant correlations with other SMTs (Table S3) while those for the SE-Dome (Table S4) and Aurora (Table S5) sites show no correlation with the other SMTs. The SMT_{REC} for the Belukha site shows no correlation with SMT_{BIAS} but a moderate correlation with Akkem SMT_{STA} ($p < 0.05$, Table S6). The SMT_{BIAS} shows significant correlations with the SMT_{STA} at the nearby stations for all sites.

The relationships among the annual values of SMT_{REC} , of positive degree day sum (PDD), and of melt layer thickness (MLT) are depicted in Figure 6. Quadratic approximations for SMT_{REC} (Figure 6a) and linear regressions for PDD (Figure 6b) well represent the relationships among variables. The relationships between SMT_{REC} and MLT are similar for Sigma-A and Aurora, cold-shifted for SE-Dome, and warm-shifted for

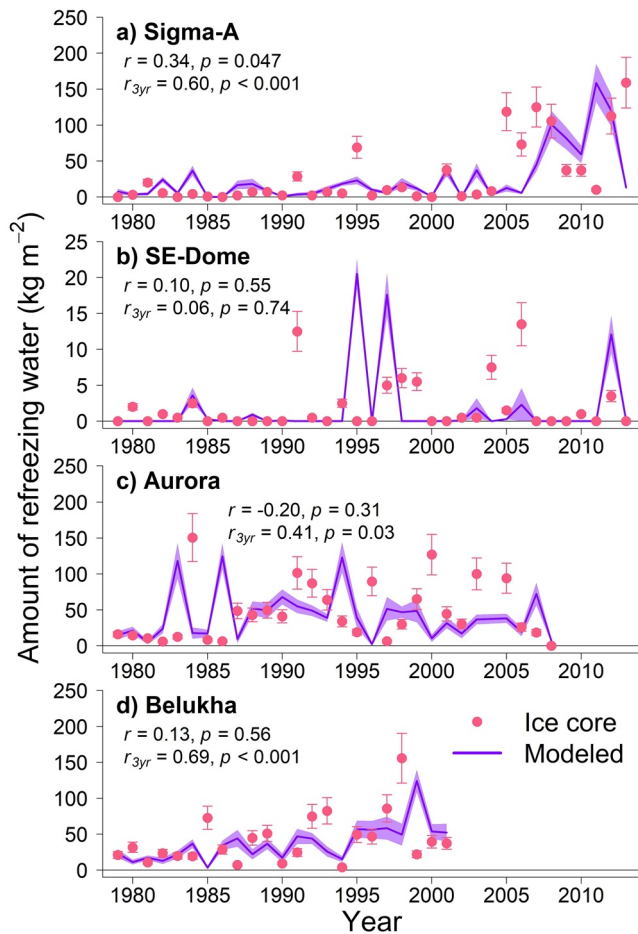


Figure 3. Observed (red circles, ice core) and simulated (purple lines) amount of refreezing water for the four ice cores: (a) Sigma-A, (b) SE-Dome, (c) Aurora, and (d) Belukha. The error bars for the ice core and shaded regions for simulated amount of refreezing water were derived from the assumed firn density before refreezing. r and r_{3yr} denote the correlation coefficients of annual and 3-year running mean refreezing amounts.

Belukha (Figure 6a). On the other hand, the relationships between PDD and MLT seem different; similar for Sigma-A and SE-Dome, cold-shifted for Aurora, and warm-shifted for Belukha (Figure 6b). The different tendency among the variables are caused by the relationships between SMT_{REC} and PDD (Figure 6c) showing that, even in the same SMT_{REC} , greater PDD will be yielded at Sigma-A and SE-Dome than at Aurora and Belukha. The idealized meteorological data suggests that the relationship between SMT and PDD is controlled by the annual temperature range (R_T).

3.3. Sensitivity to Climatic Variables

We conduct sensitivity analyses to understand what climatic features of input meteorological variables affect the relationship between MLT and estimated SMT (SMT_{SENS} , Figure 7). The SMT_{SENS} is insensitive to latitude (Figures S5 and 7a), precipitation concentration (Figures S7 and 7b), and precipitation seasonality (Figures S8 and 7c), whereas variations in the annual temperature range (Figures S6 and 7e) and firn albedo (Figure 7f) yield significant changes in the SMT_{SENS} , even if the same MLT (20 mm) and accumulation (500 mm w.e.) are used. The annual precipitation amount also significantly influences the SMT_{SENS} (Figures S9 and 7d).

Another sensitivity test that involved varying the 15 model parameters reveals that the largest SMT uncertainty is attributable to firn albedo (1.28°C), followed by fresh-snow albedo (0.29°C), the threshold air temperature for rain probability (0.28°C), and the parameter k_{min} (0.22°C) though the uncertainty values depend on the choice of the tested ranges (Table S1). These results agree reasonably well with the importance of the firn albedo, as shown above (Figure 7f). Most other parameters contribute to SMT uncertainties by $< 0.01^\circ\text{C}$. Water content, which is expected to affect the refreezing process significantly, does not affect the SMT uncertainty even when the value is varied from 3% to 10%.

4. Discussion

4.1. Uncertainty in the Reconstructed SMT

The reconstructed SMT (SMT_{REC}) includes errors resulting from the assumed firn density and seasonal patterns of the input meteorological variables. The estimated error is expressed as a quadratic sum of both errors because these are independent of each other (Section 2.1.3) and spans the range 0.65°C – 1.57°C (σ_T , Table S7). The errors derived from the assumed density (σ_d) and seasonal pattern (σ_s) are 0.04°C – 0.15°C , and 0.78°C – 1.57°C , respectively (Table S7). The error derived from the assumed density would increase with MLT whereas the main error for the study sites arises from the uncertainty in the input meteorological variables. Because meltwater refreezing occurs in the first annual layer in many cases, we consider that the assumed uncertainty of density is reasonable (350 – 550 kg m^{-3} , Table 1). The maximum error range due to seasonal patterns suggests that the linear relationship between melting and instrumental temperature from a nearby site, as used in previous studies, is not valid. Our approach allows the errors to be quantified in the temperature reconstruction, in contrast to previous studies (e.g., Henderson et al., 2006; Okamoto et al., 2011). However, model parameters are calibrated with the data of surface level and albedo observed solely at the Sigma-A site (Section 3.1). There is no observation to constrain parameters and thus it remains unknown if the calibrated parameters are applicable for the other sites. Even in the Sigma-A site, parameters affecting water percolation and refreezing are not calibrated and thus remain uncertain.

Meltwater percolation in firn may cause additional uncertainty. Although the meltwater can percolate through the melt layer in the model, the thick (refrozen) melt layer could act as a barrier to further

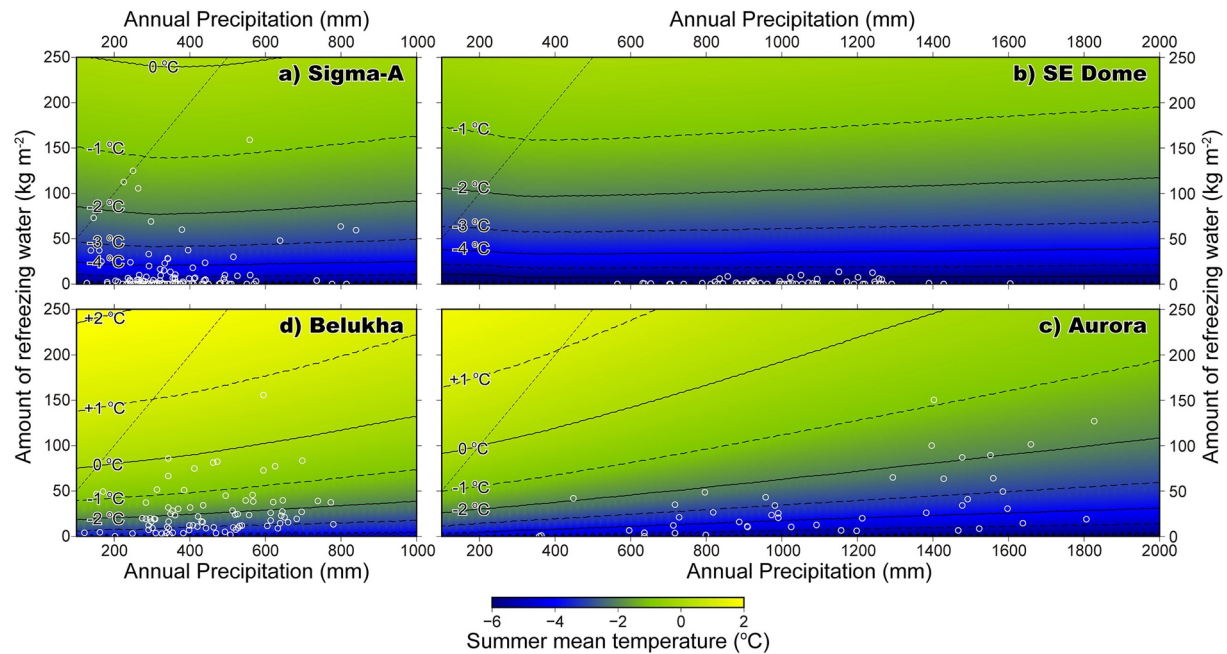


Figure 4. Calibration tables for summer mean temperature against annual precipitation (horizontal axes) and amount of refreezing water (vertical axes) for the four ice-core sites: (a) Sigma-A, (b) SE-Dome, (c) Aurora, and (d) Belukha. The open white circles denote the ice-core data for each respective site. Melt layer thickness was converted by assuming ice density (900 kg m^{-3}) and initial firn density (450 kg m^{-3}). The thin linear dashed lines denote the 100% melt feature percentage, which implies that one annual layer consists entirely of refrozen ice for a layer with an initial firn density of 450 kg m^{-3} .

percolation, as recently highlighted in Greenland (e.g., MacFerrin et al., 2019; Machguth et al., 2016; Vandecrux et al., 2020). As such, the heavy melt could also have caused water percolation and refreezing into deeper and older firn, which could yield large uncertainty. Annual layers fully consisting of ice could have formed under such events (orange bars in Figure 5). In addition, meltwater percolation is not spatially homogeneous and its modeling remains a challenging issue (e.g., Hirashima et al., 2017). If a thick melt layer prevented meltwater percolation in the model, the SMT_{REC} would be underestimated because a layer thicker than that of the present scheme would be formed under the given temperature conditions. This would cause large SMT_{REC} errors for the period during which thick melt layers were formed (orange bars in Figure 5). If excess water percolated and refroze in the deeper firn layer, it would cause a warmer bias in previous year(s) in the present scheme. In addition, with respect to water retention in firn, more realistic and complicated schemes are required to express inhomogeneous percolation and lateral flow (e.g., Hirashima et al., 2017; Vandecrux et al., 2020; Verjans et al., 2019) while water percolation in this study is simulated by a commonly used bucket water routine scheme. Nevertheless, we cannot distinguish whether a melt layer has formed in the uppermost annual layer or in deeper firn with percolated water. It is a fundamental assumption that, in an ice core analysis, melt layers should have formed within their corresponding annual layer.

Identification of melt layers is another issue that would cause an uncertainty in the SMT_{REC} . Although we defined the bubble-free layer in firn as the melt layer, it may have formed by processes other than melting, such as wind scouring or atmospheric inversion (Fegyveresi et al., 2018). Identifying the origin of these layers would require detailed in situ investigations (Fegyveresi et al., 2018) and analysis of their noble-gas chemistry (Orsi et al., 2015). Nevertheless, as a sensitivity test, we recalculate SMT_{REC} with alternative data from which thin (1-mm) melt layers are removed by assuming that such thin layers were formed as wind crusts (Figure S12). Impact of the assumption is limited in the study sites, except for the SE-Dome site where minimal values of SMT_{REC} are calculated in more summers. This is because the SE-Dome firn core contains many thin melt layers.

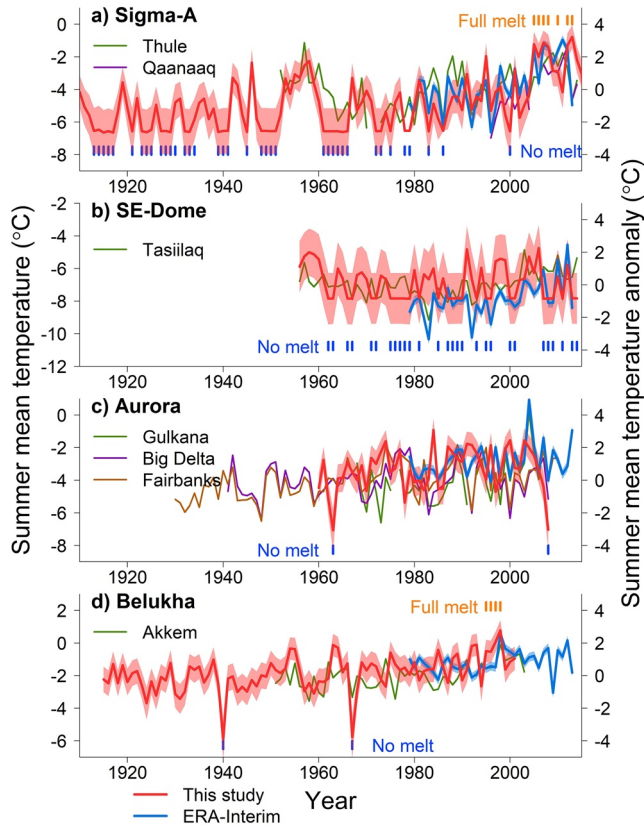


Figure 5. Reconstructed and ERA-biased summer mean temperature (SMT_{REC} and SMT_{BIAS}) from the four ice cores: (a) Sigma-A, (b) SE-Dome, (c) Aurora, and (d) Belukha. The SMTs correspond to the left y-axis, whereas the SMT anomalies of the nearby stations correspond to the right y-axis. The light-blue shaded regions for SMT_{BIAS} denote the error associated with the assumed firn density, and the light-red shaded regions for SMT_{REC} denote the errors associated with the assumed firn density and multi-year seasonal patterns of the input meteorological variables. The annual layers without melt layer (blue bars) and with fully refrozen ice (orange bars) are also shown.

4.2. Feasibility of the Method

The RMSEs and MEs of the calculated refreezing amount using the ERA-Interim temperature at the four ice-core sites are displayed in Figure S11. There is no significant minimum to the RMSEs, which suggests that the calculated refreezing amounts are not always consistent with the observed melt layers, as zero refreezing could result in a flat RMSE in colder conditions. However, periods with greater refreezing amount seem to be well represented in Sigma-A (2007–2013), Aurora (1988–1995, 2003–2006), and Belukha (1992–2002) (Figure 3). Correlation coefficients between the observed and modeled amounts of refreezing water are not better than 0.340 (Sigma-A, $p < 0.05$). This is probably due to: 1) less reliability of the ERA-Interim data at the ice core site, and 2) uncertainty of ice core dating. Nevertheless, the correlation coefficients of the 3-year running means range between 0.411 and 0.687 ($p < 0.05 \sim 0.001$) except for the SE-Dome core ($r = 0.061$). These improved correlations suggest that the long-term trend such as the recent warming is consistent between the ice-core-derived and modeled melt layers, though the interannual variability is not well represented due to the reasons above. The SE-Dome ice core seems to contain too few melt layers to apply this method.

The calibration tables for the four ice core sites show different color appearances (Figure 4). Although the calibration tables for Sigma-A and SE-Dome appear similar, the ice-core data (accumulation and refreezing amount) are plotted in different domains on the tables (Figures 4a and 4b). The different temperature distributions imply that the reconstructed SMT_{REC} differ among the sites, even for the same melt layer thickness (MLT), with colder SMTs at the two Greenland sites and warmer SMTs at Aurora and Belukha (the warmest site). Conversely, the same amount of meltwater (and refreezing) occurs at lower temperatures in Greenland compared with Alaska and Russian Altai mountains. In the two calibration tables for Greenland, the temperature isolines are almost horizontal, suggesting that the amount of annual accumulation does not affect the relationship between MLT and SMT (Figures 4a and 4b). In contrast, the inclined temperature isolines in the calibration tables for Aurora and Belukha suggest that the SMT_{REC} are affected by annual accumulation, even if the same MLT is found (Figures 4c and 4d). Namely, the SMT_{REC} will be lower in case of the larger annual accumulation.

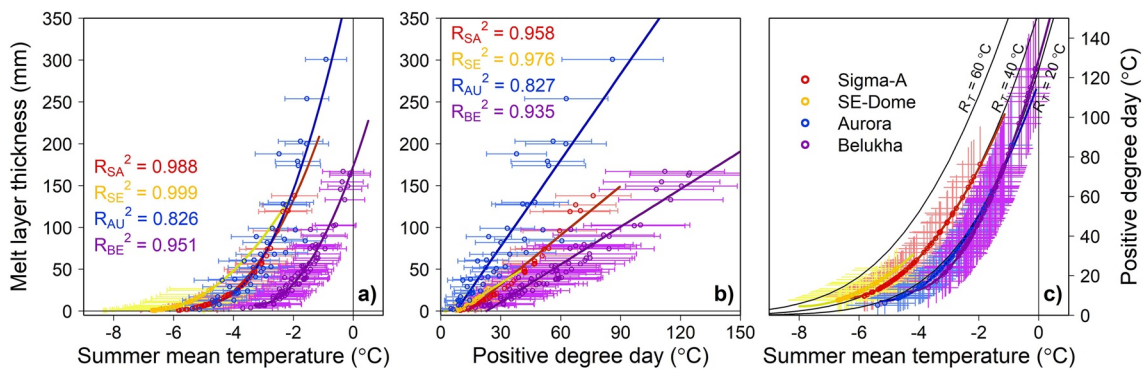


Figure 6. Relationships between (a) reconstructed summer mean temperature (SMT_{REC}) and melt layer thickness (MLT), and (b) positive degree day (PDD) and MLT of the four ice cores, and (c) SMT and PDD. Error bars denote the errors associated with the assumed firn density and meteorological patterns. R_{site}^2 denotes the coefficient of determination for regression line at the site such as SA: Sigma-A, SE: SE-Dome, AU: Aurora, and BE: Belukha. Thin black lines in (c) denote the relationships estimated from the idealized meteorological data with different annual temperature range (R_T).

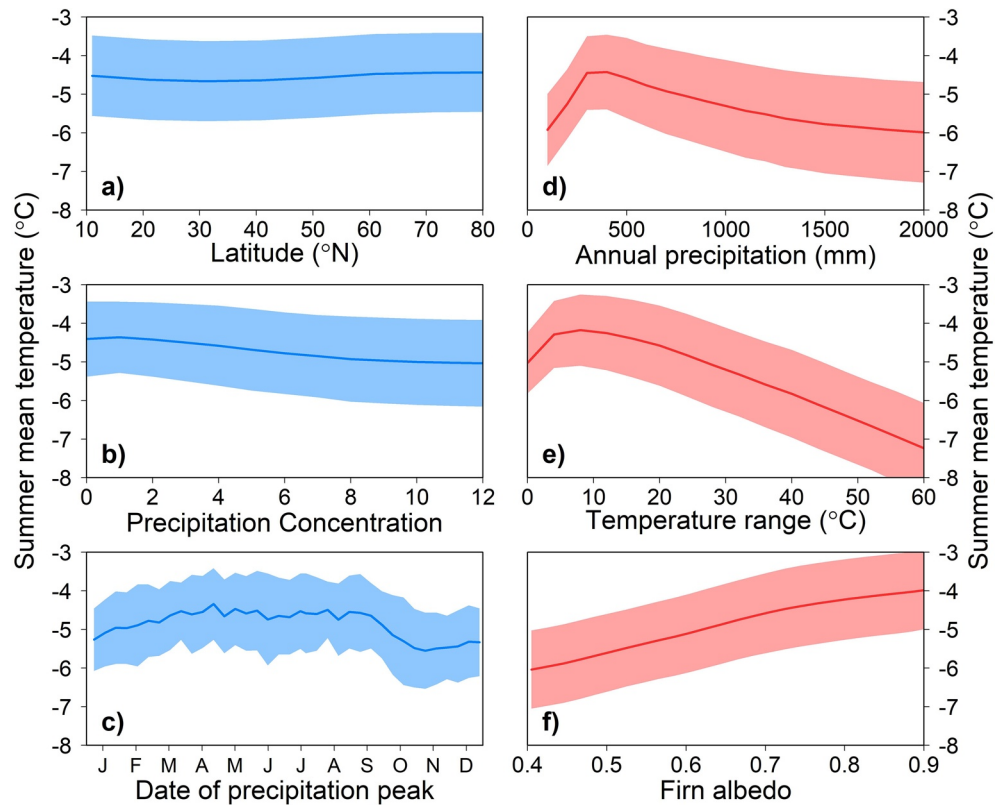


Figure 7. Sensitivity of the estimated SMTs to the following variables: (a) latitude, (b) precipitation concentration, (c) date of precipitation peak (precipitation seasonality), (d) annual precipitation, (e) temperature range, and (f) firn albedo. We assumed a 20-mm-thick melt layer and 500 mm w.e. annual accumulation (except for the sensitivity to (d) annual precipitation). Ineffective parameters are depicted in blue while effective ones are depicted in red. The shaded regions denote the estimation errors associated with the assumed firn density and year of calculation.

If winter cooling could not refreeze all retained water, the thermal condition of firn would be temperate and then the percolated water could distribute not only within the annual layer but also in the deeper and older firn. The upper left side of the calibration table, at which the refreezing water is more than annual precipitation, represents such the temperate condition. However, the combination of annual accumulation and MLT analyzed from the ice cores (Figure 4) and the borehole temperatures (Table 1) suggest that the firn preserves cold content at all sites. This issue should be noted when this method is applied to warmer sites.

Figure 5a shows that the model successfully reproduces the warm periods at Sigma-A since 2000 and during the 1950s, whereas the temperature bottoms out in the 1960s and before the 1940s, for which no melt layer is commonly observed. A similar feature (i.e., a bottomed-out temperature and no melt layer) is also found in the SE-Dome temperature (Figure 5b). It suggests a limitation of this method by which SMT cannot be estimated for the year without melt layer. Although of limited frequency, annual layers without melt layer are also found in the Aurora and Belukha ice cores (Figures 5c and 5d). Conversely, an annual layer that consisted entirely of ice could have a large uncertainty because the excess percolated water could have refrozen in a deeper/older firn layer, and could also have run off to lower elevations. Even with any other method, however, it would not be possible to obtain a precise temperature from an ice core that has been affected by substantial melting. A thick melt layer could also result in horizontal movement of percolated water in the firn layer, which could disturb the firn structure and preserved climatic/atmospheric information. Heavy melt event in 2012 could have disturbed the information of accumulation and refreezing in the firn across the entire Greenland (e.g., Nghiem et al., 2012; Niwano et al., 2015).

The SMT_{REC} shows significant correlations with the nearby station SMT_{STA} for the Sigma-A and Belukha sites (Table S3 and S6) but no correlation for the SE-Dome and Aurora sites (Tables S4 and S5). The uncorrelated temperatures, which could be due to few melt layers contained in the SE-Dome ice core, suggest the

limitation of this method as mentioned above (Figure 5b and Table S4). On the other hand, the uncorrelated temperatures for the Aurora ice core could be due to uncertainty in ice-core dating because the correlation coefficients are significantly improved when the 3-year running means are compared ($r = 0.319 \sim 0.433$, Table S5). Considering the inconsistent relationships among the Alaskan station data, Big Delta and Fairbanks may not be appropriate sites for the validation. SMT_{REC} for the Belukha site shows no correlation with SMT_{BIAS} but with the Akkem and SO11 temperatures (Table S6). SMT_{REC} and SO11 are significantly correlated, but not in perfect agreement, even though they are based on the same data of melt layer thickness. This is due to the fact that SO11 is based on a linear relationship between temperature and melt layer thickness, whereas that for SMT_{REC} is nonlinear. The good correlations among SMTs for the Sigma-A site may be the result of the parameter calibration of the model. To estimate SMT at an ice-core site, where observational data is basically unavailable, some degree of parameter adjustments is needed but it should not be over-tuned for avoiding a site-specific bias.

The direct relationships between MLT and SMT are similar for the Sigma-A and Aurora sites (Figure 6a), even though the calibration tables (Figures 4a and 4c), and the MLT and PDD (Figure 6b) exhibit similar features only for the two Greenland sites. The inconsistency may be attributed to the relationships between SMT and PDD (Figure 6c). The idealized climate variables suggest that the SMT-PDD relationship is regulated by the annual temperature range (R_T). The rather simple relationship between PDD and snow melt is attributed to the significant contribution of downward longwave radiation to the energy budget over the snow surface (Ohmura, 2001). Based on this concept, Winski et al. (2018) converted the melt amounts, which were estimated from MLT, to SMT (July and August in their study) by assuming a linear relationship between PDD and melt, and a normal distribution of daily temperatures for converting PDD into SMT. Although the results of our analysis also show that PDD affects the snow melt linearly, the relationship differs site by site. In addition, the SMT-PDD relationship would further alter the relationship between SMT and snow melt. It suggests that, to better understand the relationship between temperature and snow melt, we have to analyze those among SMT, PDD and snow melt. Variation of the points around the corresponding approximate curve or line could be affected by variability of the other climatic factors such as annual accumulation.

4.3. Comparison With Water Stable Isotopic Compositions

To demonstrate the feasibility of the proposed method and the traditional method of inferring temperature from isotopes, we compare the SMT_{REC} , SMT_{BIAS} , and annual averages of deuterium isotopes (WSI) in the four ice cores (Figure S13). The interannual variability of deuterium isotopes differs from site to site, being large at the Sigma-A and Belukha sites, and small at the SE-Dome and Aurora sites. Fluctuations and trends in deuterium isotope are different to those of SMT at the same site. No correlation is found between WSI and SMTs (Tables S3–S6) except for that between the Belukha WSI and Akkem SMT_{STA} (Table S6). The inconsistency between SMT and WSI can be attributed to variability of vapor source, seasonality of precipitation, meltwater percolation, and post-depositional change. SMT contains information about summer conditions while the annual WSI signal could be affected by winter accumulation and seasonal variability of precipitation, though the main precipitation season seems to be summer at the study sites, except for the SE-Dome site (Figure S3c). However, even when the summer mean deuterium isotope and temperatures are compared for the SE-Dome and Belukha ice cores, which are dated in monthly and semi-annual cycles, respectively, no correlation is found (not shown). In addition, the dating uncertainty should affect the inconsistency between the SMT_{BIAS} and WSI. The WSI approach requires observational temperature data to convert WSI to temperature as well as the empirical approach based on melt layers while our new method can estimate SMT without instrumental record. Despite these discrepancies, we consider that it is meaningful to provide alternative and independent temperature information by our method.

4.4. Parameters Affecting the Reconstructed SMT

The results of the sensitivity simulation suggest that the estimated SMT_{SENS} increases as annual precipitation increases until 400 mm (Figure 7d). More precipitation would keep the surface albedo higher and thus warmer temperature is required to produce the same amount of meltwater. On the other hand, the SMT_{SENS} falls along with increasing annual precipitation if higher than 400 mm. Heat and mass budget analysis

suggests that rain input proportionally increases with annual precipitation if the SMT is unchanged. It implies that, to yield the same thickness of melt layer, the SMT_{SENS} has to decrease with the increase of annual precipitation.

The likelihood of high positive temperatures during the summer increases as temperature range increases. Such warming events would result in the formation of meltwater and subsequent refreezing, such that the SMT_{SENS} could be lower (Figure 7e). A slight drop in the SMT_{SENS} around the zero temperature range is caused by a necessity to reduce the probability of rain. This suggests that the temperature range of reanalysis data should be reliable at an ice core site, even if the representativeness of temperature and precipitation were uncertain. In addition, variability of the temperature range in the past could cause a large uncertainty in the estimated SMT.

Firn albedo as a boundary condition shows an obvious positive correlation with the SMT_{SENS} (Figure 7f). It can be explained by a change in the energy budget of the snow surface. A lower albedo could enhance snow melting even under lower temperature environment and vice versa. This suggests that improvement of the albedo scheme is required for a more precise estimation of SMT. In addition, to apply this method to Asian ice cores, which contain more impurities such as dust and black carbon than those in other regions (Ginot et al., 2014; Takeuchi et al., 2009), we have to know how much albedo was reduced with a dusty layer found in an ice core. The timing of dust deposition is also important because snowfall or melting events following the deposition would drastically alter the surface albedo (Fujita, 2007; Fujita et al., 2011).

Change in latitude does not affect SMT_{SENS} (Figure 7a) while it largely alters the seasonality of solar radiation (Figure S5). The heat and mass budget analysis suggests that, at a high accumulation zone where ice cores are drilled, the summertime solar radiation and thus the net shortwave radiation vary little with latitude.

Although it has been pointed out that precipitation concentration and seasonality strongly influenced glacier mass balance and its response to temperature change in sensitivity analyses previously conducted (Fujita, 2008; Fujita & Ageta, 2000; Sakai & Fujita, 2017), these variables do not show any significant influence on the temperature estimation (Figures 7b and 7c). The heat and mass budget analysis suggests that, whether due to concentration or seasonality, there is not only a decrease in melt amount through higher albedo conditions, but also an increase in rain water input. These conflicting responses compensate and then yield the same refreezing amount.

5. Conclusion

In this study, we offered a novel method to estimate summer mean temperature (SMT) from melt layers in an ice core with a physical background. In contrast to traditional and empirical approaches, this method allows us to estimate SMT using only ice-core information, meaning that an approximate relationship between the observed local temperature and melt layer is not required. Despite the lack of a strong correlation between the SMTs reconstructed by this method and those observed at nearby stations, some significant features and trends (e.g., warm periods and recent warming) were well reproduced for three of the ice core sites. However, the reconstructed SMTs at the cold, high-accumulation site in southeastern Greenland were inconsistent with observed temperatures because the conditions were generally too cold to produce meltwater. The temperature range over which SMTs can be reconstructed using this method is likely to be -6°C to $+1^{\circ}\text{C}$. In addition, the quadratic relationship between SMT and melt layer thickness varies under different climate regimes. Sensitivity analyses suggest that the annual temperature range and annual precipitation amount have a significant influence on the relationship between the SMT and melt layer thickness, among which the annual precipitation amount is available as a fundamental information (as accumulation rate). Therefore, both the accuracy of annual temperature range in the reanalysis data set and the assumption of a constant annual temperature range in the past are crucial for estimating reliable SMT. Firn albedo, which was assumed to be invariant over time as a boundary condition, is also important to estimate summer mean temperature precisely. We analyzed only firn cores in this study, from which the melt layers were easily identified. Further work requires a method for extracting the melt layer from deeper ice.

Data Availability Statement

Accumulation and melt layer thickness of four ice cores used in this study are provided in the supporting information. Observational air temperature data are available through the website of National Centers for Environmental Information in National Oceanic and Atmospheric Administration (<https://www.ncdc.noaa.gov/>), and of Cappelen (2016). Access URLs for individual data are listed in Table S2. The ERA-Interim reanalysis data were downloaded from the ECMWF server (<https://apps.ecmwf.int/sso/login/openid-connect/>).

Acknowledgments

T. Aoki was supported by the GCOM-C/SGLI Mission of JAXA. This study was supported by MEXT/JSPS KAKENHI (26257201, 18H05292, 23221004, 16H01772, and 15H01733), and the Joint Research Program of the Institute of Low Temperature Science, Hokkaido University. The authors are grateful to the thoughtful comments from V. Verjans and an anonymous reviewer.

References

- Aizen, E. M., Aizen, V. B., Takeuchi, N., Mayewski, P. A., Grigholm, B., Joswiak, D. R., et al. (2016). Abrupt and moderate climate changes in the mid-latitudes of Asia during the Holocene. *Journal of Glaciology*, *62*(233), 411–439. <https://doi.org/10.1017/jog.2016.34>
- Alley, R. B., & Anandakrishnan, S. (1995). Variations in melt-layer frequency in the GISP2 ice core: Implications for Holocene summer temperatures in central Greenland. *Annals of Glaciology*, *21*, 64–70. <https://doi.org/10.3189/S0260305500015615>
- Aoki, T., Matoba, S., Uetake, J., Takeuchi, N., & Motoyama, H. (2014). Field activities of the “snow impurity and glacial microbe effects on abrupt warming in the arctic” (sigma) project in Greenland in 2011–2013. *Bulletin of Glaciological Research*, *32*, 3–20. <https://doi.org/10.5331/bgr.32.3>
- Cappelen, J. (Ed.). (2016). *Greenland—DMI historical climate data collection 1784–2015*. Copenhagen: Danish Meteorological Institute.
- Dee, D. P., Uppala, S. M., Simmons, A. J., Berrisford, P., Poli, P., Kobayashi, S., et al. (2011). The era-interim reanalysis: Configuration and performance of the data assimilation system. *The Quarterly Journal of the Royal Meteorological Society*, *137*(656), 553–597. <https://doi.org/10.1002/qj.828>
- Epstein, S., Sharp, R. P., & Goddard, I. (1963). Oxygen-isotope ratios in Antarctic snow, firn, and ice. *The Journal of Geology*, *71*(6), 698–720. <https://doi.org/10.1086/626950>
- Fegyveresi, J. M., Alley, R. B., Muto, A., Orsi, A. J., & Spencer, M. K. (2018). Surface formation, preservation, and history of low-porosity crusts at the WAIS divide site, west Antarctica. *The Cryosphere*, *12*(1), 325–341. <https://doi.org/10.5194/tc-12-325-2018>
- Fisher, D. A., & Koerner, R. M. (1994). Signal and noise in four ice-core records from the Agassiz ice cap, Ellesmere Island, Canada: Details of the last millennium for stable isotopes, melt and solid conductivity. *The Holocene*, *4*(2), 113–120. <https://doi.org/10.1177/095968369400400201>
- Fujita, K. (2007). Effect of dust event timing on glacier runoff: Sensitivity analysis for a Tibetan glacier. *Hydrological Processes*, *21*(21), 2892–2896. <https://doi.org/10.1002/hyp.6504>
- Fujita, K. (2008). Effect of precipitation seasonality on climatic sensitivity of glacier mass balance. *Earth and Planetary Science Letters*, *276*(1–2), 14–19. <https://doi.org/10.1016/j.epsl.2008.08.028>
- Fujita, K., & Ageta, Y. (2000). Effect of summer accumulation on glacier mass balance on the Tibetan plateau revealed by mass-balance model. *Journal of Glaciology*, *46*(153), 244–252. <https://doi.org/10.3189/172756500781832945>
- Fujita, K., Ageta, Y., Pu, J., & Yao, T. (2000). Mass balance of xiao dongkemadi glacier on the central Tibetan Plateau from 1989 to 1995. *Annals of Glaciology*, *31*, 159–163. <https://doi.org/10.3189/172756400781820075>
- Fujita, K., & Nuimura, T. (2011). Spatially heterogeneous wastage of Himalayan glaciers. *Proceedings of the National Academy of Sciences of the United States of America*, *108*(34), 14011–14014. <https://doi.org/10.1073/pnas.1106242108>
- Fujita, K., Ohta, T., & Ageta, Y. (2007). Characteristics and climatic sensitivities of runoff from a cold-type glacier on the Tibetan Plateau. *Hydrological Processes*, *21*(21), 2882–2891. <https://doi.org/10.1002/hyp.6505>
- Fujita, K., & Sakai, A. (2014). Modelling runoff from a Himalayan debris-covered glacier. *Hydrology and Earth System Sciences*, *18*(7), 2679–2694. <https://doi.org/10.5194/hess-18-2679-2014>
- Fujita, K., Seko, K., Ageta, Y., Pu, J., & Yao, T. (1996). Superimposed ice in glacier mass balance on the Tibetan Plateau. *Journal of Glaciology*, *42*(142), 454–460. <https://doi.org/10.3189/S0022143000003440>
- Fujita, K., Takeuchi, N., Nikitin, S., Surazakov, A., Okamoto, S., Aizen, V., & Kubota, J. (2011). Favorable climatic regime for maintaining the present-day geometry of the Gregoriev glacier, inner Tien Shan. *The Cryosphere*, *5*(3), 539–549. <https://doi.org/10.5194/tc-5-539-2011>
- Furukawa, R., Uemura, R., Fujita, K., Sjolte, J., Yoshimura, K., Matoba, S., & Iizuka, Y. (2017). Seasonal-scale dating of a shallow ice core from Greenland using oxygen isotope matching between data and simulation. *Journal of Geophysical Research*, *122*(20), 10. <https://doi.org/10.1002/2017JD026716>
- Ginot, P., Dumont, M., Lim, S., Patris, N., Taupin, J.-D., Wagnon, P., et al. (2014). A 10 year record of black carbon and dust from a Mera peak ice core (Nepal): Variability and potential impact on melting of Himalayan glaciers. *The Cryosphere*, *8*(4), 1479–1496. <https://doi.org/10.5194/tc-8-1479-2014>
- Henderson, K., Laube, A., Gäggeler, H. W., Olivier, S., Papina, T., & Schwikowski, M. (2006). Temporal variations of accumulation and temperature during the past two centuries from Belukha ice core, Siberian Altai. *Journal of Geophysical Research*, *111*(D3), D03104. <https://doi.org/10.1029/2005JD005819>
- Herron, M. M., Herron, S. L., & Langway, C. C. (1981). Climatic signal of ice melt features in southern Greenland. *Nature*, *293*(5831), 389–391. <https://doi.org/10.1038/293389a0>
- Hirashima, H., Avanzi, F., & Yamaguchi, S. (2017). Liquid water infiltration into a layered snowpack: Evaluation of a 3-d water transport model with laboratory experiments. *Hydrology and Earth System Sciences*, *21*(11), 5503–5515. <https://doi.org/10.5194/hess-21-5503-2017>
- Iizuka, Y., Matoba, S., Yamasaki, T., Oyabu, I., Kadota, M., & Aoki, T. (2016). Glaciological and meteorological observations at the se-dome site, southeastern Greenland ice sheet. *Bulletin of Glaciological Research*, *34*, 1–10. <https://doi.org/10.5331/bgr.15R03>
- Iizuka, Y., Miyamoto, A., Hori, A., Matoba, S., Furukawa, R., Saito, T., et al. (2017). A firn densification process in the high accumulation dome of southeastern Greenland. *Arctic Antarctic and Alpine Research*, *49*(1), 13–27. <https://doi.org/10.1657/AAAR0016-034>
- Iizuka, Y., Uemura, R., Fujita, K., Hattori, S., Seki, O., Miyamoto, C., et al. (2018). A 60 year record of atmospheric aerosol depositions preserved in a high-accumulation dome ice core, southeast Greenland. *Journal of Geophysical Research*, *123*(1), 574–589. <https://doi.org/10.1002/2017JD026733>
- Johnsen, S. J., Dahl-Jensen, D., Gundestrup, N., Steffensen, J. P., Clausen, H. B., Miller, H., et al. (2001). Oxygen isotope and palaeotemperature records from six Greenland ice-core stations: Camp Century, Dye-3, GRIP, GISP2, Renland and northgrip. *Journal of Quaternary Science*, *16*(4), 299–307. <https://doi.org/10.1002/jqs.622>

- Jouzel, J., Alley, R. B., Cuffey, K. M., Dansgaard, W., Grootes, P., Hoffmann, G., et al. (1997). Validity of the temperature reconstruction from water isotopes in ice cores. *Journal of Geophysical Research*, *102*(C12), 26471–26487. <https://doi.org/10.1029/97JC01283>
- Kameda, T., Narita, H., Shoji, H., Nishio, F., Fujii, Y., & Watanabe, O. (1995). Melt features in ice cores from site j, southern Greenland: Some implications for summer climate since ad 1550. *Annals of Glaciology*, *21*, 51–58. <https://doi.org/10.3189/S0260305500015597>
- Koerner, R. M. (1977). Devon Island ice cap: Core stratigraphy and paleoclimate. *Science*, *196*(4285), 15–18. <https://doi.org/10.1126/science.196.4285.15>
- Koerner, R. M., & Fisher, D. (1990). A record of Holocene summer climate from a Canadian high-arctic ice core. *Nature*, *343*(6259), 630–631. <https://doi.org/10.1038/343630a0>
- Kondo, J. (Ed.). (1994). *Meteorology of the water environment-water and heat balance of the Earth's surface*. Tokyo: Asakura Shoten Press. (in Japanese).
- Kurita, N., Yoshida, N., Inoue, G., & Chayanova, E. A. (2004). Modern isotope climatology of Russia: A first assessment. *Journal of Geophysical Research*, *109*(D3), D03102. <https://doi.org/10.1029/2003JD003404>
- Kurosaki, Y., Matoba, S., Iizuka, Y., Niwano, M., Tanikawa, T., Ando, T., et al. (2020). Reconstruction of sea ice concentration in northern Baffin Bay using deuterium excess in a coastal ice core from the northwestern Greenland ice sheet. *Journal of Geophysical Research*, *125*(16), e2019JD031668. <https://doi.org/10.1029/2019JD031668>
- MacFerrin, M., Machguth, H., van As, D., Charalampidis, C., Stevens, C. M., Heilig, A., et al. (2019). Rapid expansion of Greenland's low-permeability ice slabs. *Nature*, *573*(7774), 403–407. <https://doi.org/10.1038/s41586-019-1550-3>
- Machguth, H., MacFerrin, M., van As, D., Box, J. E., Charalampidis, C., Colgan, W., et al. (2016). Greenland meltwater storage in firn limited by near-surface ice formation. *Nature Climate Change*, *6*(4), 390–393. <https://doi.org/10.1038/nclimate2899>
- Matoba, S., Niwano, M., Tanikawa, T., Iizuka, Y., Yamasaki, T., Kurosaki, Y., et al. (2018). Field activities at the sigma-a site, northwestern Greenland ice sheet, 2017. *Bulletin of Glaciological Research*, *36*, 15–22. <https://doi.org/10.5331/bgr.18R01>
- Matsuda, Y., Fujita, K., Ageta, Y., & Sakai, A. (2006). Estimation of atmospheric transmissivity of solar radiation from precipitation in the Himalaya and the Tibetan Plateau. *Annals of Glaciology*, *43*, 344–350. <https://doi.org/10.3189/172756406781812177>
- Mellor, M. (1977). Engineering properties of snow. *Journal of Glaciology*, *19*(81), 15–66. <https://doi.org/10.3189/S002214300002921X>
- Nghiem, S., Hall, D., Mote, T., Tedesco, M., Albert, M., Keegan, K., et al. (2012). The extreme melt across the Greenland ice sheet in 2012. *Geophysical Research Letters*, *39*(20), L20502. <https://doi.org/10.1029/2012GL053611>
- Nishimura, M., Aoki, T., Niwano, M., Matoba, S., Tanikawa, T., Yamaguchi, S., & Kurosaki, Y. (2021). *Quality-controlled datasets of automatic weather station (AWS) at sigma-A site from 2012 to 2020, 1.30*. Japan: Arctic Data Archive System (ADS). Retrieved from <https://ads.nipr.ac.jp/data/meta/A20210318-002/>
- Niwano, M., Aoki, T., Hashimoto, A., Matoba, S., Yamaguchi, S., Tanikawa, T., et al. (2018). NHM-SMAP: Spatially and temporally high-resolution nonhydrostatic atmospheric model coupled with detailed snow process model for Greenland ice sheet. *The Cryosphere*, *12*(2), 635–655. <https://doi.org/10.5194/tc-12-635-2018>
- Niwano, M., Aoki, T., Matoba, S., Yamaguchi, S., Tanikawa, T., Kuchiki, K., & Motoyama, H. (2015). Numerical simulation of extreme snowmelt observed at the sigma-A site, northwest Greenland, during summer 2012. *The Cryosphere*, *9*(3), 971–988. <https://doi.org/10.5194/tc-9-971-2015>
- Ohmura, A. (2001). Physical basis for the temperature-based melt-index method. *Journal of Applied Meteorology*, *40*(4), 753–761. [https://doi.org/10.1175/1520-0450\(2001\)040<3C0753:PBFTTB>3E2.0.CO;2](https://doi.org/10.1175/1520-0450(2001)040<3C0753:PBFTTB>3E2.0.CO;2)
- Okamoto, S., Fujita, K., Narita, H., Uetake, J., Takeuchi, N., Miyake, T., et al. (2011). Reevaluation of the reconstruction of summer temperatures from melt features in Belukha ice cores, Siberian Altai. *Journal of Geophysical Research*, *116*, D02110. <https://doi.org/10.1029/2010JD013977>
- Orsi, A. J., Kawamura, K., Fegyveresi, J. M., Headly, M. A., Alley, R. B., & Severinghaus, J. P. (2015). Differentiating bubble-free layers from melt layers in ice cores using noble gases. *Journal of Glaciology*, *61*(227), 585–594. <https://doi.org/10.3189/2015JG14J237>
- Pfahl, S., & Sodemann, H. (2014). What controls deuterium excess in global precipitation? *Climate of the Past*, *10*(2), 771–781. <https://doi.org/10.5194/cp-10-771-2014>
- Sakai, A., & Fujita, K. (2017). Contrasting glacier responses to recent climate change in high-mountain Asia. *Scientific Reports*, *7*(1), 13717. <https://doi.org/10.1038/s41598-017-14256-5>
- Sakai, A., Fujita, K., Narama, C., Kubota, J., Nakawo, M., & Yao, T. (2010). Reconstructions of annual discharge and equilibrium line altitude of glaciers at Qilian Shan, northwest china, from 1978 to 2002. *Hydrological Processes*, *24*(19), 2798–2806. <https://doi.org/10.1002/hyp.7700>
- Sakai, A., Nuimura, T., Fujita, K., Takenaka, S., Nagai, H., & Lamsal, D. (2015). Climate regime of Asian glaciers revealed by Gamdam glacier inventory. *The Cryosphere*, *9*(3), 865–880. <https://doi.org/10.5194/tc-9-865-2015>
- Steig, E. J., Grootes, P. M., & Stuiver, M. (1994). Seasonal precipitation timing and ice core records. *Science*, *266*(5192), 1885–1886. <https://doi.org/10.1126/science.266.5192.1885>
- Takeuchi, N., Miyake, T., Nakazawa, F., Narita, H., Fujita, K., Sakai, A., et al. (2009). A shallow ice core re-drilled on the Dunde ice cap, western china: Recent changes in the Asian high mountains. *Environmental Research Letters*, *4*(4), 045207. <https://doi.org/10.1088/1748-9326/4/4/045207>
- Takeuchi, N., Takahashi, A., Uetake, J., Yamasaki, T., Aizen, V. B., Joswiak, D., & Nikitin, S. A. (2004). A report on ice core drilling on the western plateau of Mt. Belukha in the Russian Altai Mountains in 2003. *Polar Meteorology and Glaciology*, *18*, 121–133.
- Trusel, L. D., Das, S. B., Osman, M. B., Evans, M. J., Smith, B. E., Fettweis, X., et al. (2018). Nonlinear rise in Greenland runoff in response to post-industrial arctic warming. *Nature*, *564*(7734), 104–108. <https://doi.org/10.1038/s41586-018-0752-4>
- Tsushima, A., Matoba, S., Shiraiwa, T., Okamoto, S., Sasaki, H., Solie, D., & Yoshikawa, K. (2015). Reconstruction of recent climate change in Alaska from the Aurora peak ice core, central Alaska. *Climate of the Past*, *11*(2), 217–226. <https://doi.org/10.5194/cp-11-217-2015>
- Vandecrux, B., Mottram, R., Langen, P. L., Fausto, R. S., Olesen, M., Stevens, C. M., et al. (2020). The firn meltwater Retention Model Inter-comparison Project (RETMIP): Evaluation of nine firn models at four weather station sites on the Greenland ice sheet. *The Cryosphere*, *14*, 3785–3810. <https://doi.org/10.5194/tc-14-3785-2020>
- Verjans, V., Leeson, A. A., Stevens, C. M., MacFerrin, M., Noël, B., & Broeke, M. R. (2019). Development of physically based liquid water schemes for Greenland firn-densification models. *The Cryosphere*, *13*(7), 1819–1842. <https://doi.org/10.5194/tc-13-1819-2019>
- Wever, N., Würzer, S., Fierz, C., & Lehning, M. (2016). Simulating ice layer formation under the presence of preferential flow in layered snowpacks. *The Cryosphere*, *10*(6), 2731–2744. <https://doi.org/10.5194/tc-10-2731-2016>
- Winski, D., Osterberg, E., Kreutz, K., Wake, C., Ferris, D., Campbell, S., et al. (2018). A 400-year ice core melt layer record of summertime warming in the Alaska Range. *Journal of Geophysical Research*, *123*(7), 3594–3611. <https://doi.org/10.1002/2017JD027539>

Supporting Information for Physically based summer temperature reconstruction from melt layers in ice cores

Koji Fujita, Sumito Matoba, Yoshinori Iizuka, Nozomu Takeuchi,
Akane Tsushima, Yutaka Kurosaki, and Teruo Aoki

Contents of this file

1. Captions for Datasets S1 to S2
2. Methods
3. Figures S1 to S13
4. Tables S1 and S7
5. References

Data Set S1: dso1.csv Annual accumulation (acc, mm w.e.) and melt layer thickness (mlt, mm) of the ice-cores at SA:Sigma-A, SE:SE-Dome, AU:Aurora, and BE:Belukha, respectively.

Data Set S2: dso2.csv Summer mean temperature observed at the Akkem station (see Table S2).

1 Methods

1.1 Albedo

As solar radiation is the main heat source for snow melting, the albedo estimate has a strong influence on the modeled generation of meltwater, and therefore refreezing water. We utilize a scheme proposed by Kondo and Xu (1997) to estimate the temporal change in daily surface albedo (α_d , dimensionless), which is calculated as follows:

$$\alpha_d = (\alpha_{d-1} - \alpha_f)e^{-1/k} + \alpha_f, \quad (S1)$$

here α_{d-1} and α_f are the albedos of the previous day and firn, respectively, and k is a parameter that expresses the exponential decrease in surface snow albedo with time. The number of days since the last fresh snow is set to zero ($d = 0$) when the snowfall is greater than a threshold amount (P_{S_min} , mm w.e.). The surface snow albedo reduces exponentially with time, with k depending on air temperature of (T_a , °C) as follows:

$$k = \max \left[k_{min}; k_{min} + \frac{dk}{dT}(T_a - T_t) \right], \quad (S2)$$

here k_{min} , T_t , and dk/dT are the minimum value of k , threshold air temperature that yields k_{min} , and a negative slope ($< 0 \text{ } ^\circ\text{C}^{-1}$) at a temperature lower than T_t , respectively. The albedo of fresh snow (α_0 , dimensionless) also depends on the air temperature when snowfall occurs as:

$$\begin{aligned}
\alpha_0 &= \alpha_{max} & [T_a < T_{min}], \\
&= \frac{(\alpha_f - \alpha_{max})(T_a - T_{min})}{T_{max} - T_{min}} + \alpha_{max} & [T_{min} \leq T_a \leq T_{max}], \\
&= \alpha_f & [T_a > T_{max}],
\end{aligned} \tag{S3}$$

here α_{max} is the albedo of fresh and cold snow, T_{min} and T_{max} are the threshold air temperatures for the albedo of the falling snow. The surface albedo is affected by a darker firn when the snow layer is thin. If we assume that solar radiation penetrates through the snow layer via Fick's second law of diffusion (Giddings and LaChapelle; 1961), the surface snow albedo (α_s) over the underlying firn (α_f) can be calculated as follows:

$$\begin{aligned}
\alpha_s &= \frac{2 - w(1 - y)}{2 + w(1 - y)}, \\
w &= \frac{2(1 - \alpha_d)}{1 + \alpha_d}, \\
y &= \frac{[2(1 - \alpha_f) - w(1 + \alpha_f)]e^{-\mu_s D_s}}{-w(1 + \alpha_f) \cosh(\mu_s D_s) - 2(1 - \alpha_f) \sinh(\mu_s D_s)},
\end{aligned} \tag{S4}$$

here D_s is the snow layer thickness above the firn surface (m), and μ_s is the extinction coefficient of snow (m^{-1}) (Greuell and Konzelmann; 1994).

1.2 Densification of snow layers

The change in snow thickness above the firn, which affects the surface albedo, as described in Eq. (S4), is calculated as the change in snow density for a daily time step as:

$$\frac{1}{\rho_z} \frac{d\rho_z}{dt} = \frac{\sum \rho_z dz}{\eta_z}, \tag{S5}$$

here ρ_z is the snow density ($kg\ m^{-3}$) at depth of z (m) and η_z is the snow viscosity ($kg\ m^{-2}\ day$). This change is calculated with the overburden load from depth z to the surface ($\sum \rho_z dz$, $kg\ m^{-2}$). The snow viscosity is described as follows:

$$\eta_z = f_w \eta_c e^{c_d \rho_z}, \tag{S6}$$

here η_c and c_d are constants ($kg\ m^{-2}\ day$ and $m^3\ kg^{-1}$, respectively), and f_w is a parameter that depends on the presence of water, which is set to 1.0 when no water exists (Fujita; 2007). The density and thickness of snow layers varied temporally based on the snow densification process, which incorporates the snow viscosity and overburden load at a given snow layer. Details of the model are described in Fujita and Ageta (2000), Fujita et al. (2007), and Fujita and Sakai (2014).

All parameter values from Eqs. (S1) to (S6) are determined via the Monte Carlo simulation described in the Sect. 2.2.4.

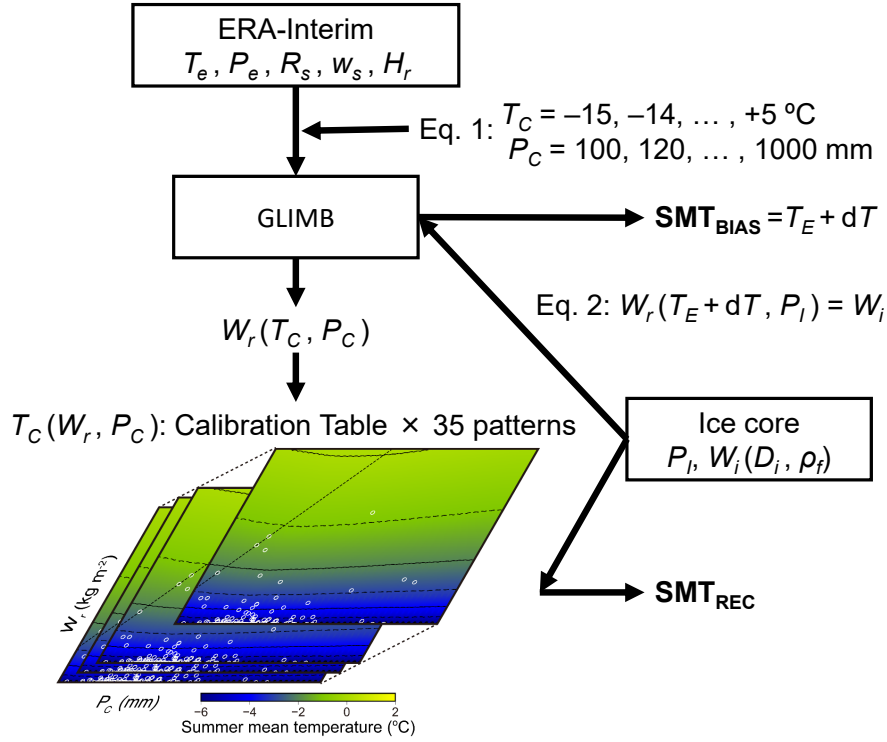


Figure S1 Block diagram for estimating the reconstructed summer mean temperature (SMT_{REC}) and the biased ERA-temperature (SMT_{BIAS}). T_e, P_e, R_s, w_s, H_r denote daily values of air temperature, precipitation, solar radiation, wind speed, and relative humidity in the ERA-Interim reanalysis data. T_C and P_C denote summer mean temperature and annual precipitation to regulate the input variables in Eq. (1). W_r is the calculated amount of refreezing water. P_I and D_i denote annual accumulation and melt layer thickness obtained from ice core analysis. W_i is refreezing amount converted from melt layer thickness with an assumed firn density (ρ_f). dT is temperature bias that yield zero mean error between W_i and W_r .

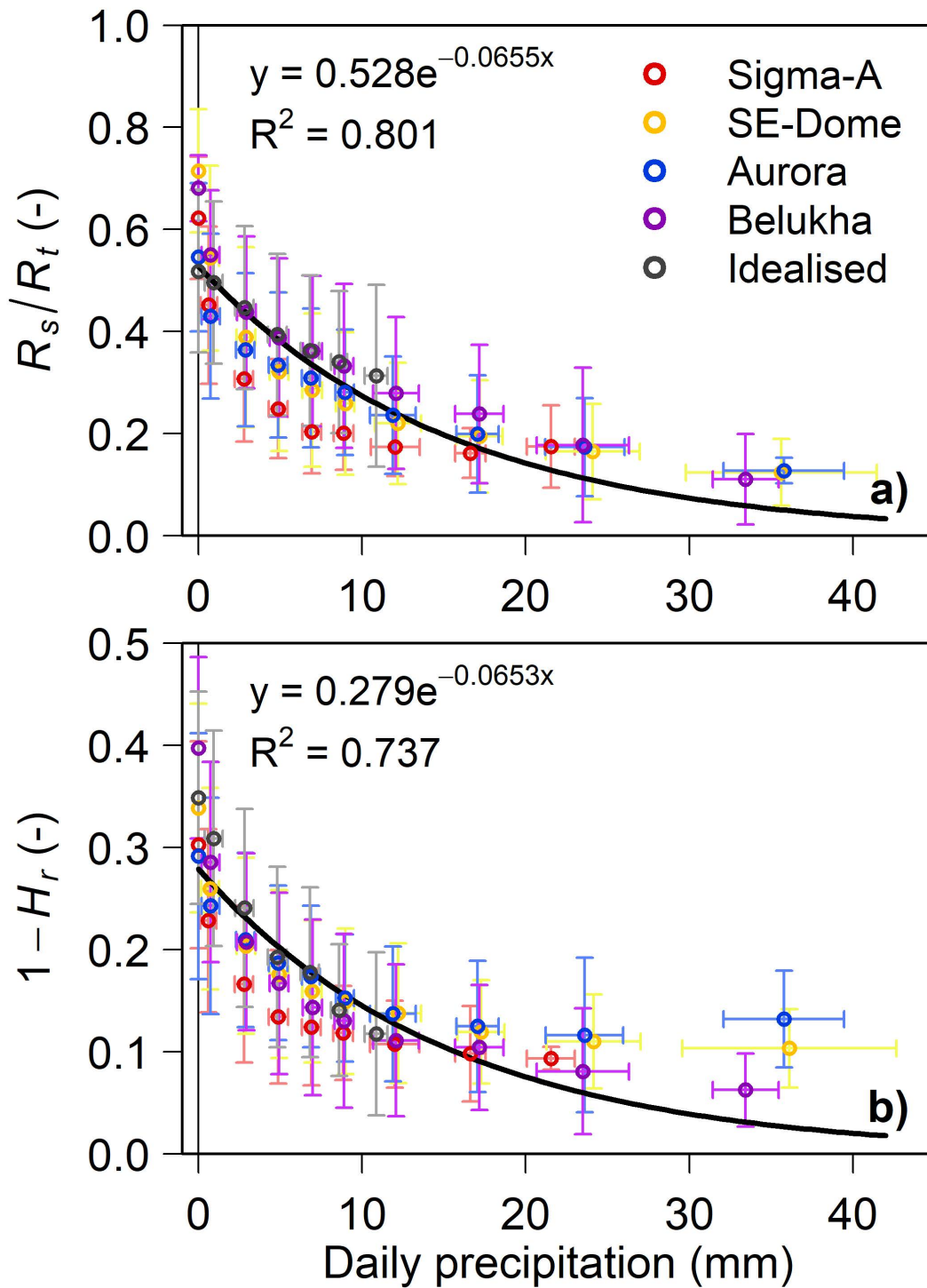


Figure S2 Relationships between daily precipitation and (a) normalised solar radiation (R_s/R_t) and (b) the residual of the relative humidity ($1 - H_r$) for the four ice-core sites and idealised settings for the sensitivity analysis (black circles). The best-fit exponential curves (black lines) were calculated from all the data from the four ice-core sites. The error bars denote the standard deviations for each data section.

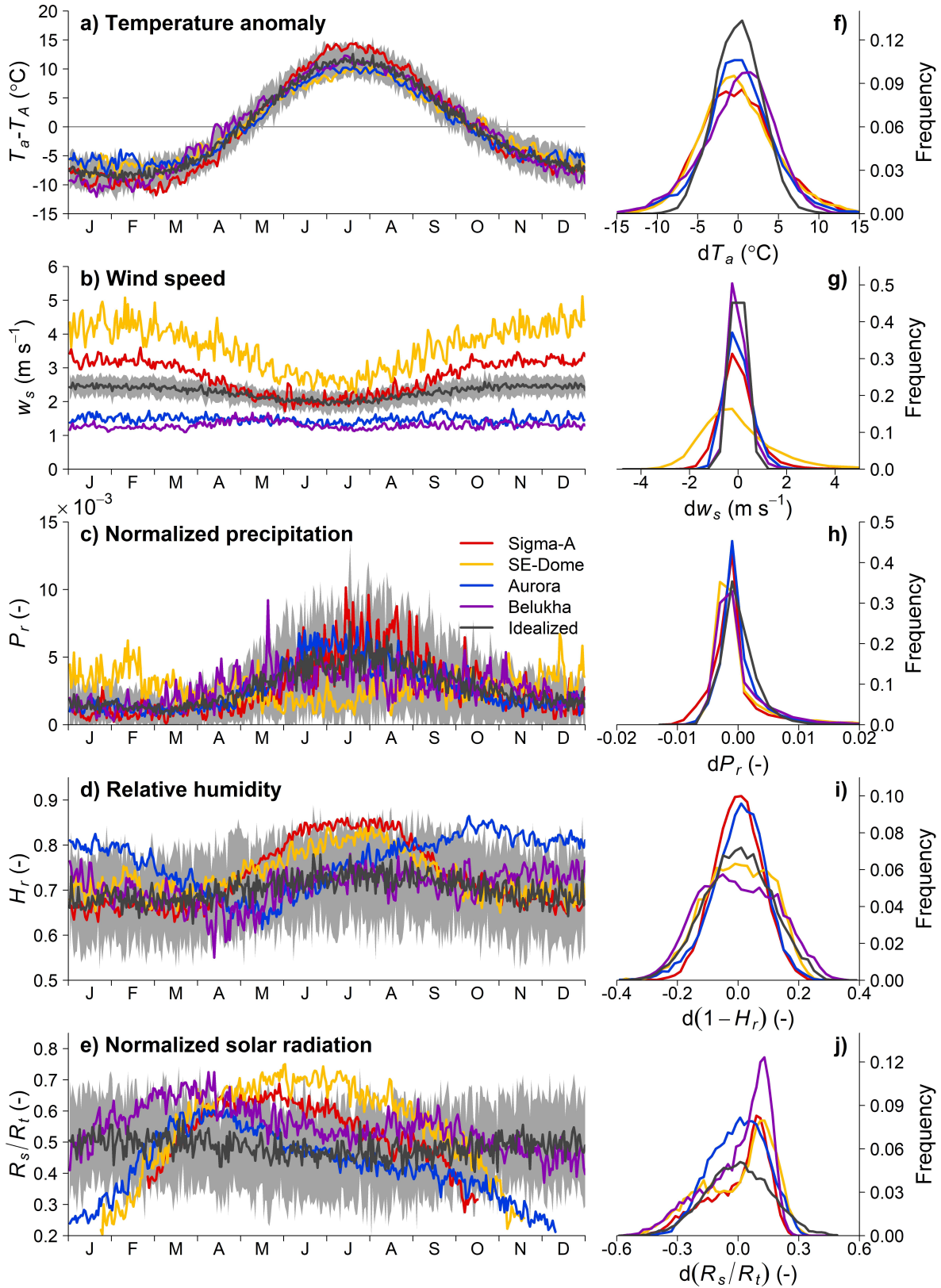


Figure S3 Long-term seasonal patterns of (a) air temperature anomaly ($T_a - T_A$), (b) wind speed (w_s), (c) normalised precipitation (P_r), (d) relative humidity (H_r), and (e) normalised solar radiation (R_s/R_t). (f-j) Histograms of the daily anomalies in the long-term patterns of the respective variables. The coloured lines denote ERA-Interim data for the four ice-core sites. The black lines with grey shaded regions denote the idealised variables for the sensitivity analysis.

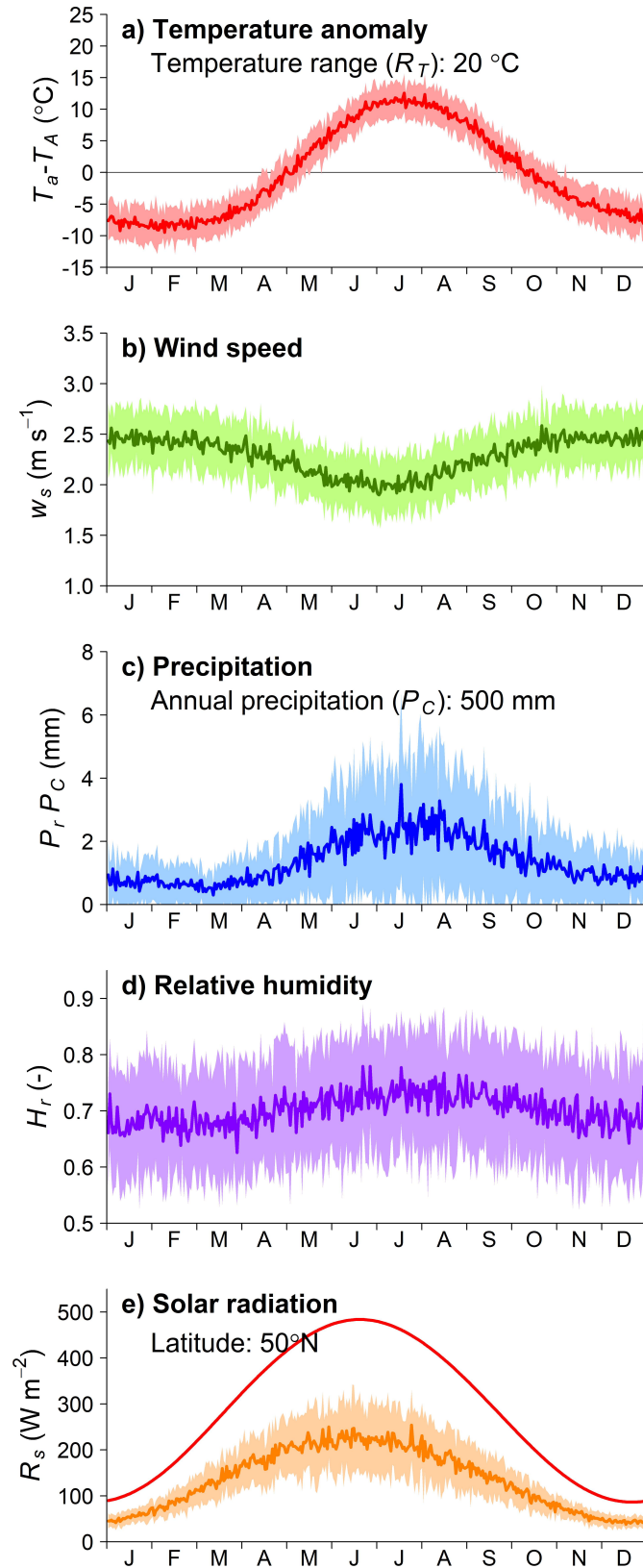


Figure S4 Standard settings of (a) air temperature anomaly ($T_a - T_A$), (b) wind speed (w_s), (c) precipitation ($P_r P_C$), (d) relative humidity (H_r), and (e) solar radiation (R_s) for the sensitivity analysis. The shaded regions denote the interannual variability. The smoothed red line in (e) denotes the solar radiation at the top of the atmosphere.

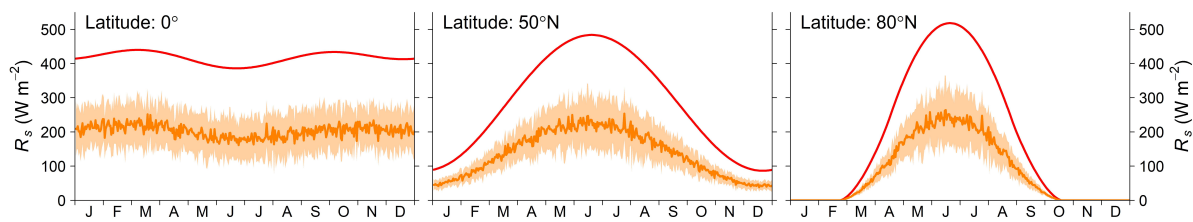


Figure S5 Examples of downward solar radiation (orange lines) affected by changing latitude for the sensitivity analysis. The shaded regions denote the interannual variability. The smoothed red lines denote the solar radiation at the top of the atmosphere.

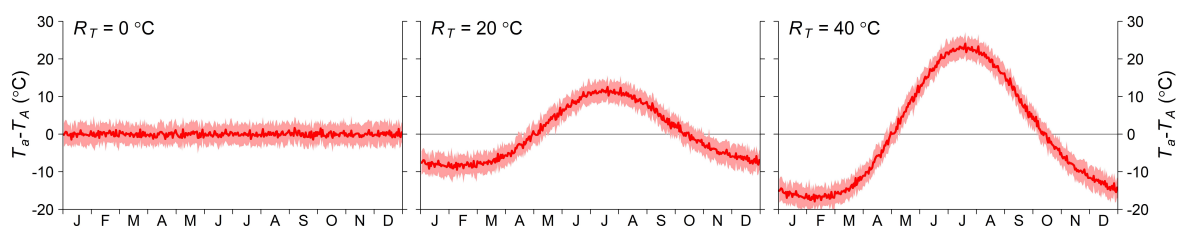


Figure S6 Examples of varying temperature range (R_T) for the sensitivity analysis. The shaded regions denote the interannual variability.

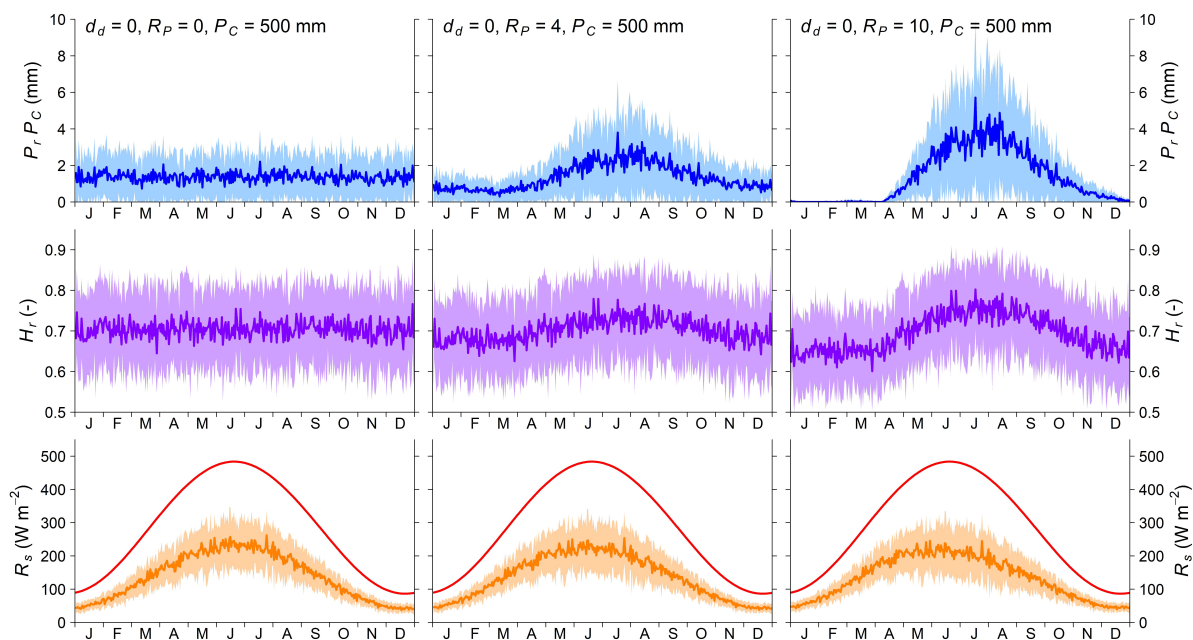


Figure S7 Examples of varying precipitation concentration (R_p) for the sensitivity analysis. Not only precipitation (P_r , P_C) but also relative humidity (H_r) and solar radiation (R_s) are affected. The shaded regions denote the interannual variability. The smoothed red lines in the solar radiation plots denote the solar radiation at the top of the atmosphere.

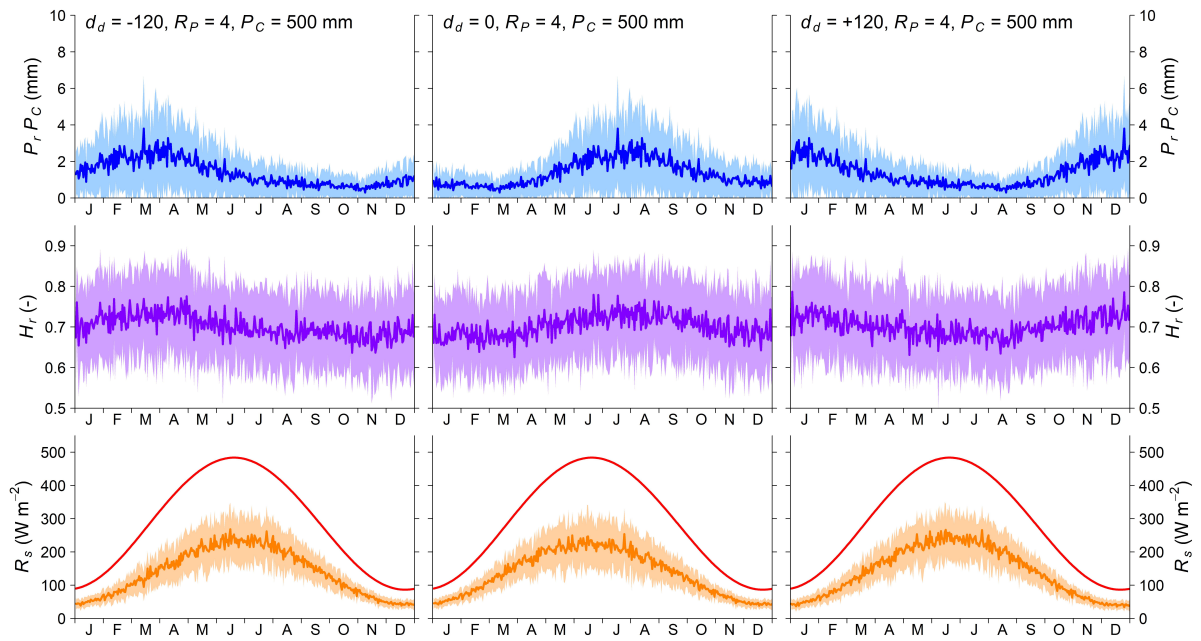


Figure S8 As Fig. S7, but for varying precipitation seasonality (d_d).

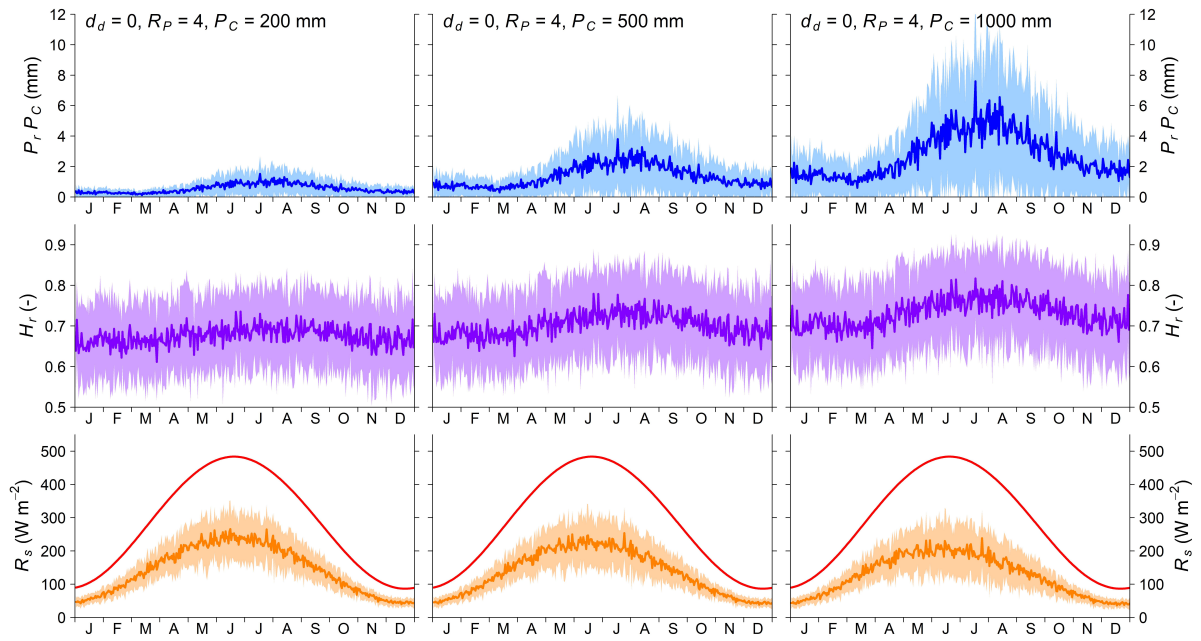


Figure S9 As Fig. S7, but for varying annual precipitation amount (P_C).

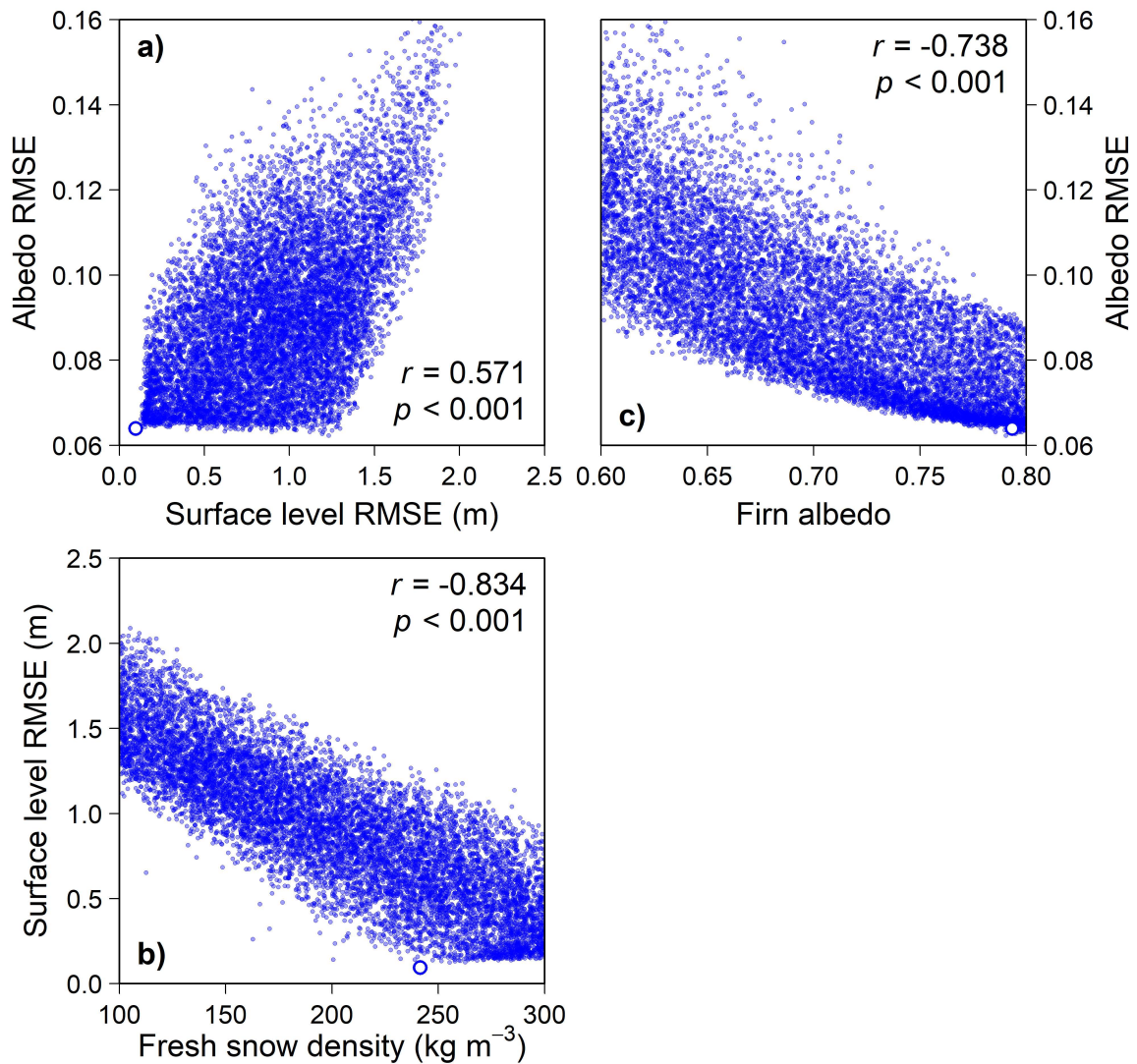


Figure S10 Scatter plots of the Monte Carlo simulation ($n = 10,000$), showing the highest correlations between (a) surface level and albedo RMSEs, (b) fresh snow density and surface level RMSEs, and (c) firn albedo and albedo RMSEs. The open circles denote the parameters that yield the best estimate of the surface level RMSE.

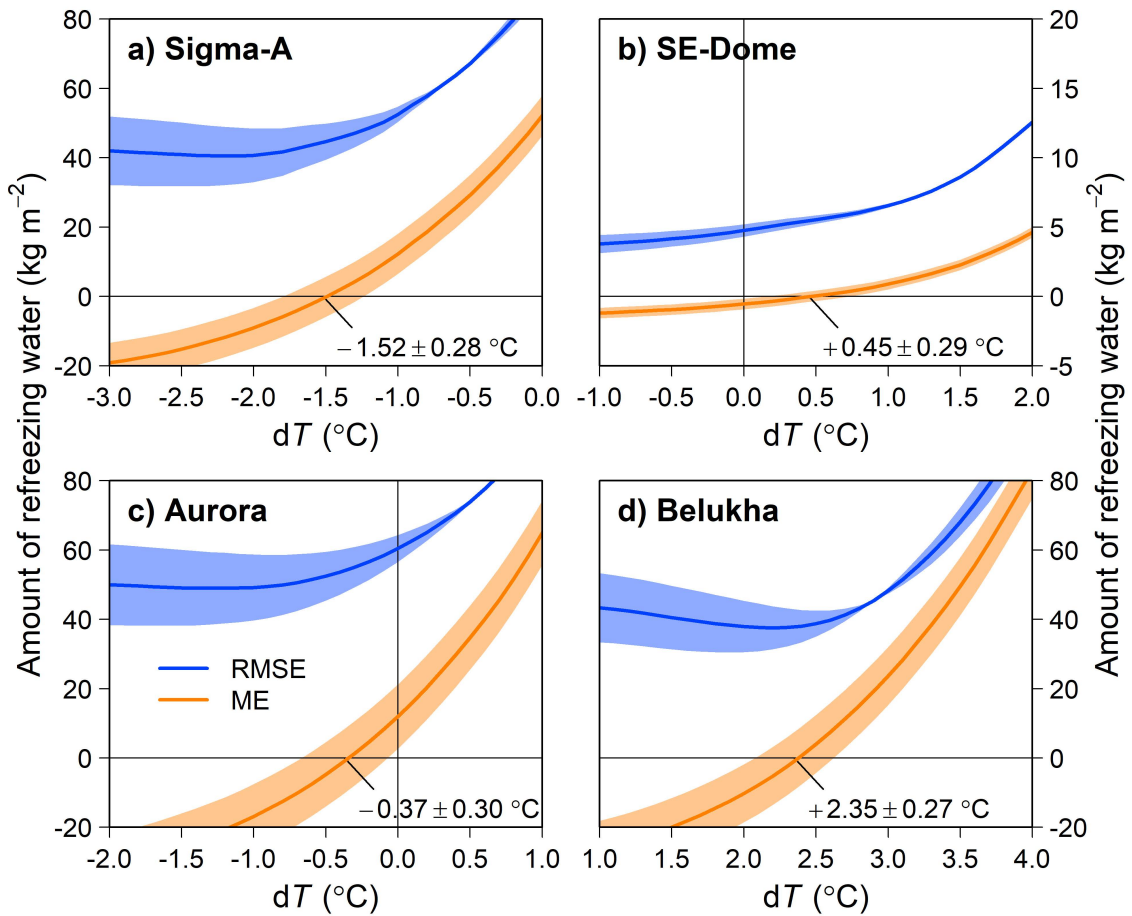


Figure S11 Root mean square error (RMSE) and mean error (ME) of the calculated amount of refreezing water using the ERA-Interim dataset at the four ice-core sites. The temperature where ME equals to zero was adopted to calculate the biased ERA-temperature (SMT_{BIAS}). The shaded regions denote the errors associated with the assumed firn density (Sect. 2.1.3).

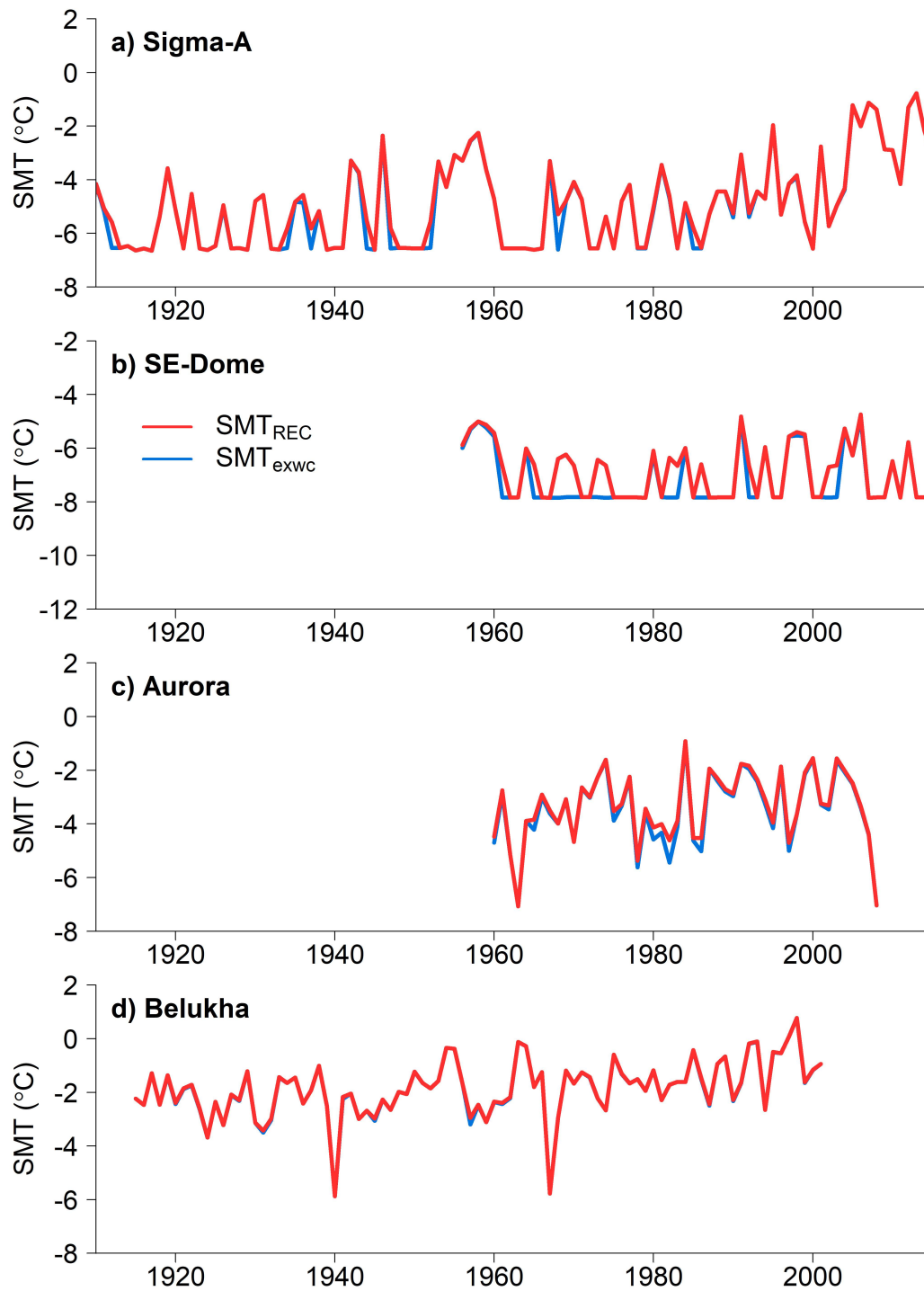


Figure S12 Reconstructed summer mean temperature (SMT) based on the approach of this study (SMT_{REC}) and that from a modified melt layer thickness, from which 1-mm thick layers are removed (SMT_{exwc}).

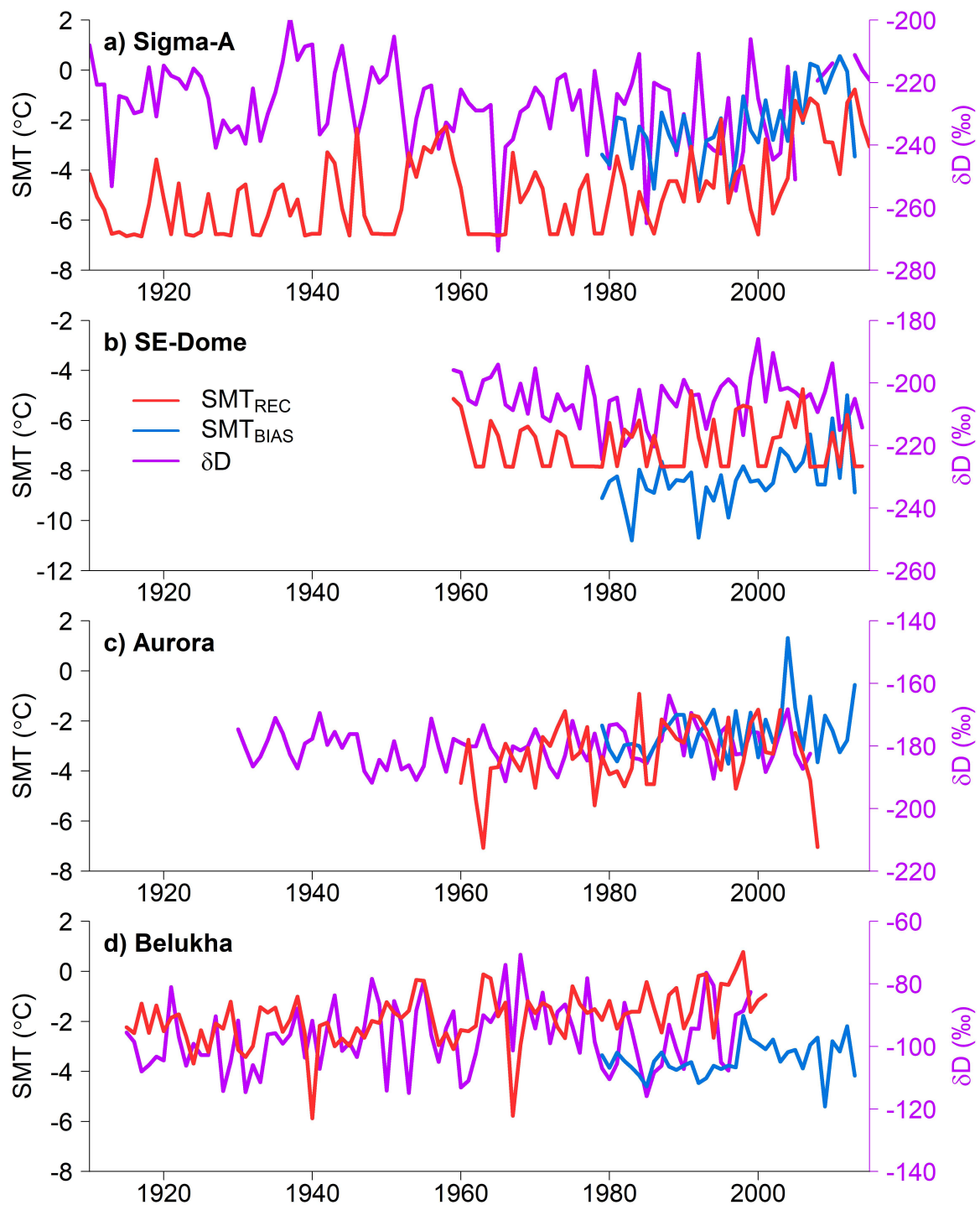


Figure S13 Reconstructed (SMT_{REC} , red lines) and ERA-biased (SMT_{BIAS} , light blue) summer mean temperatures (left axes), and deuterium isotope (purple, right axes) from (a) Sigma-A, (b) SE-Dome, (c) Aurora, and (d) Belukha ice-core sites. Ranges in temperature and deuterium isotope scales are uniform among the sites ($10\text{ }^{\circ}\text{C}$ for SMT axes and $80\text{ }‰$ for deuterium axes).

Table S1 Parameters tested in the Monte Carlo simulation.

Parameter	Symbol/Unit/Eq.	Tested range	Best estimate value	r with RMSE of level	RMSE of surface	r with RMSE of albedo	SMT uncertainty (°C)
Fresh snow density	ρ_n , kg m ⁻³	1.00~3.00	241	-0.834 ^a		-0.171	0.00
Maximum water content	w_c , %	4.0~6.0	4.17	-0.004		0.002	0.00
Threshold temperature for rain probability	T_r , °C	3.0~5.0	3.00	-0.007		-0.005	0.28
Threshold precipitation amount for resetting albedo	P_{S_min} , mm w.e.	1.0~5.0	4.77	0.042		0.216	0.06
Firn albedo	α_f , -, Eq. S1	0.6~0.8	0.793	-0.436 ^a		-0.738 ^a	1.28
Minimum value of albedo parameter k	k_{min} , -, Eq. S2	3.0~5.0	4.65	-0.014		-0.021	0.22
Threshold temperature for albedo parameter	T_t , °C, Eq. S2	-0.5~1.5	0.129	-0.062		-0.088	0.08
Slope gradient for albedo parameter k	dk/dT , °C ⁻¹ , Eq. S2	-4.0~-2.0	-2.03	-0.025		-0.116	0.01
Fresh snow albedo	α_{max} , -, Eq. S3	0.8~0.9	0.897	-0.096		-0.482 ^a	0.29
Minimum threshold temperature for fresh snow albedo	T_{min} , °C, Eq. S3	-2.0~0.0	-1.82	-0.004		-0.011	0.01
Maximum threshold temperature for firn albedo	T_{max} , °C, Eq. S3	2.0~4.0	3.34	-0.003		-0.000	0.01
Parameter for albedo reduction	μ_s , -, Eq. S4	25.0~35.0	32.2	-0.004		-0.014	0.00
Parameter of water presence for snow densification	f_w , -, Eq. S6	$1.60 \sim 2.60 \times 10^{-2}$	2.44×10^{-2}	-0.254		0.011	0.00
Parameter for snow viscosity	η_c , kg m ⁻² , Eq. S6	14.0~18.0	17.4	-0.010		-0.005	0.00
Parameter for snow viscosity	c_d , m ⁻³ kg ⁻¹ , Eq. S6	0.10~0.90	0.218	-0.006		0.009	0.00

SMT uncertainty denotes the uncertainty of reconstructed summer mean temperature (SMT) associated with the range in each parameter.

^a $p < 0.001$

Table S2 Meteorological stations nearby ice core sites used in this study.

Station name	Qaanaaq	Thule	Tasiilaq	Big Delta	Gulkana	Fairbanks	Akkem
Latitude (°N)	77.48	76.55	65.60	64.00	62.17	64.82	49.91
Longitude (°)	290.62	291.18	322.37	214.28	214.55	212.15	86.54
Altitude (m a.s.l.)	38	16	50	386	479	133	2047
Observation since	1996	1948	1895	1941	1968	1929	1951
Corresponding ice core site	Sigma-A	Sigma-A	SE-Dome	Aurora	Aurora	Aurora	Belukha
Direction and distance (km) from ice core site	SSW ₁₇₆	S ₁₇₀	SSW ₁₈₅	NE ₆₇	SSE ₁₆₀	NNW ₁₅₈	N ₁₂
Data at Qaanaaq and Tasiilaq (Cappelen; 2016): https://www.dmi.dk/fileadmin/user_upload/Rapporter/TR/2016/DMIRep16_04.zip							
Data at Thule: https://www.ncdc.noaa.gov/cdo-web/datasets/GHCND/stations/GHCND:GLW00017605/detail							
Data at Big Delta: https://www.ncdc.noaa.gov/cdo-web/datasets/GHCND/stations/GHCND:USW00026415/detail							
Data at Gulkana: https://www.ncdc.noaa.gov/cdo-web/datasets/GHCND/stations/GHCND:USW00026425/detail							
Data at Fairbanks: https://www.ncdc.noaa.gov/cdo-web/datasets/GHCND/stations/GHCND:USW00026411/detail							
Data at Akkem is provided as Data Set 2							

Table S3 Correlation coefficients among water stable isotope (WSI) and summer mean temperatures for the Sigma-A ice core. Upper-right and lower-left groups denote the results from annual and 3-year running means. SMT_{REC} and SMT_{BIAS} denote the summer mean temperature reconstructed by the method of this study and that from the biased ERA-Interim temperature, respectively. Significance levels are: ^a $p < 0.001$, ^b $p < 0.01$, ^c $p < 0.05$, ^d $p < 0.1$, respectively.

Sigma-A	WSI	SMT _{REC}	SMT _{BIAS}	Thule	Qaanaaq
WSI	–	–0.114	–0.033	0.113	0.242
SMT _{REC}	–0.142	–	0.611 ^a	0.398 ^b	0.479 ^d
SMT _{BIAS}	0.325	0.773 ^a	–	0.779 ^a	0.864 ^a
Thule	0.334 ^c	0.615 ^a	0.824 ^a	–	0.859 ^a
Qaanaaq	0.613	0.797 ^b	0.965 ^a	0.835 ^a	–

Table S4 As Table S3, but for the SE-Dome ice core.

SE-Dome	WSI	SMT _{REC}	SMT _{BIAS}	Tasiilaq
WSI	–	0.193	0.239	0.139
SMT _{REC}	0.392 ^b	–	0.226	0.073
SMT _{BIAS}	0.093	0.036	–	0.617 ^a
Tasiilaq	0.153	0.156	0.813 ^a	–

Table S5 As Table S3, but for the Aurora ice core.

Aurora	WSI	SMT _{REC}	SMT _{BIAS}	Gulkana	Big Delta	Fairbanks
WSI	–	–0.040	0.067	0.126	–0.039	–0.010
SMT _{REC}	0.012	–	0.139	0.147	–0.017	–0.046
SMT _{BIAS}	0.219	0.433 ^c	–	0.883 ^a	0.470 ^b	0.486 ^b
Gulkana	0.335 ^d	0.319 ^d	0.913 ^a	–	0.407 ^c	0.354 ^c
Big Delta	0.169	0.064	0.395 ^c	0.249	–	0.833 ^a
Fairbanks	0.167	0.243	0.369 ^c	0.125	0.802 ^a	–

Table S6 As Table S3, but for the Belukha ice core. SO₁₁ denotes the summer mean temperature reconstructed by Okamoto et al. (2011).

Belukha	WSI	SMT _{REC}	SMT _{BIAS}	Akkem	SO ₁₁
WSI	–	0.122	0.227	0.290 ^c	0.139
SMT _{REC}	0.160	–	–0.011	0.326 ^c	0.679 ^a
SMT _{BIAS}	0.116	0.303	–	0.783 ^a	0.101
Akkem	0.185	0.626 ^a	0.767 ^a	–	0.318 ^c
SO ₁₁	0.306 ^b	0.796 ^a	0.195	0.673 ^a	–

Table S7 Errors for the reconstructed SMTs (σ_T , °C), which are the quadratic sum of those derived from the assumed firn density (σ_d , °C) and the seasonal patterns of the input meteorological variables (σ_s , °C).

Ice core site	Sigma-A	SE-Dome	Aurora	Belukha
σ_T (°C)	0.65	1.57	0.85	0.76
σ_d (°C)	0.07	0.04	0.15	0.13
σ_s (°C)	1.16	1.57	0.84	0.78

References

- Cappelen, J. (ed.) (2016). *Greenland - DMI Historical Climate Data Collection 1784–2015*, Danish Meteorological Institute, Copenhagen.
- Fujita, K. (2007). Effect of dust event timing on glacier runoff: sensitivity analysis for a tibetan glacier, *Hydrol. Process.* **21**(21): 2892–2896.
- Fujita, K. and Ageta, Y. (2000). Effect of summer accumulation on glacier mass balance on the tibetan plateau revealed by mass-balance model, *J. Glaciol.* **46**(153): 244–252.
- Fujita, K., Ohta, T. and Ageta, Y. (2007). Characteristics and climatic sensitivities of runoff from a cold-type glacier on the tibetan plateau, *Hydrol. Process.* **21**(21): 2882–2891.
- Fujita, K. and Sakai, A. (2014). Modelling runoff from a himalayan debris-covered glacier, *Hydrol. Earth Sys. Sci.* **18**(7): 2679–2694.
- Giddings, J. and LaChapelle, E. (1961). Diffusion theory applied to radiant energy distribution and albedo of snow, *J. Geophys. Res.* **66**(1): 181–189.
- Greuell, W. and Konzelmann, T. (1994). Numerical modelling of the energy balance and the englacial temperature of the greenland ice sheet. calculations for the eth-camp location (west greenland, 1155 m asl), *Global Planet. Change* **9**(1-2): 91–114.
- Kondo, J. and Xu, J. (1997). Seasonal variations in the heat and water balances for nonvegetated surfaces, *J. Appl. Meteor.* **36**(12): 1676–1695.
- Okamoto, S., Fujita, K., Narita, H., Uetake, J., Takeuchi, N., Miyake, T., Nakazawa, F., Aizen, V. B., Nikitin, S. A. and Nakawo, M. (2011). Reevaluation of the reconstruction of summer temperatures from melt features in belukha ice cores, siberian altai, *J. Geophys. Res.* **116**: D02110.